The Astronomical Journal, 169:235 (26pp), 2025 May https://doi.org/10.3847/1538-3881/adbbed

The TESS–Keck Survey. XXIV. Outer Giants May Be More Prevalent in the Presence of Inner Small Planets

Judah Van Zandt[1,23], Erik A. Petigura[1], Jack Lubin[1], Lauren M. Weiss[2], Emma V. Turtelboom[3], Tara Fetherolf[4,24], Joseph M. Akana Murphy[5,25], Ian J. M. Crossfield[6], Gregory J. Gilbert[1], Teo Močnik[7], Natalie M. Batalha[8], Courtney Dressing[3], Benjamin Fulton[9], Andrew W. Howard[10], Daniel Huber[11,12], Howard Isaacson[3,13], Stephen R. Kane[4], Paul Robertson[14], Arpita Roy[15,16], Isabel Angelo[1], Aida Behmard[17,26], Corey Beard[14,23], Ashley Chontos[11,18,27], Fei Dai[5,11], Steven Giacalone[10], Michelle L. Hill[4], Rae Holcomb[14], Steve B. Howell[19], Andrew W. Mayo[1,3], Daria Pidhorodetska[4,23], Alex S. Polanski[20], James Rogers[20], Lee J. Rosenthal[10], Ryan A. Rubenzahl[21], Nicholas Scarsdale[8], Dakotah Tyler[1], Samuel W. Yee[22,28], and Jon Zink[10]

[1] Department of Physics & Astronomy, University of California Los Angeles, Los Angeles, CA 90095, USA; judahvz@astro.ucla.edu
[2] Department of Physics and Astronomy, University of Notre Dame, Notre Dame, IN 46556, USA
[3] Department of Astronomy, University of California Berkeley, Berkeley, CA 94720, USA
[4] Department of Earth and Planetary Sciences, University of California, Riverside, CA 92521, USA
[5] Department of Astronomy and Astrophysics, University of California, Santa Cruz, CA 95064, USA
[6] Department of Physics & Astronomy, University of Kansas, 1082 Malott, 1251 Wescoe Hall Drive, Lawrence, KS 66045, USA
[7] Gemini Observatory/NSF NOIRLab, 670 N. A'ohoku Place, Hilo, HI 96720, USA
[8] Department of Astronomy and Astrophysics, University of California, Santa Cruz, CA 95060, USA
[9] NASA Exoplanet Science Institute/Caltech-IPAC, MC 314-6, 1200 E. California Boulevard, Pasadena, CA 91125, USA
[10] Department of Astronomy, California Institute of Technology, Pasadena, CA 91125, USA
[11] Institute for Astronomy, University of Hawai'i, 2680 Woodlawn Drive, Honolulu, HI 96822, USA
[12] Sydney Institute for Astronomy (SIfA), School of Physics, University of Sydney, NSW 2006, Australia
[13] Centre for Astrophysics, University of Southern Queensland, Toowoomba, QLD 4350, Australia
[14] Department of Physics & Astronomy, University of California, Irvine, Irvine, CA 92697, USA
[15] Space Telescope Science Institute, 3700 San Martin Drive, Baltimore, MD 21218, USA
[16] Department of Physics and Astronomy, Johns Hopkins University, 3400 N Charles Street, Baltimore, MD 21218, USA
[17] American Museum of Natural History, 200 Central Park West, Manhattan, NY 10024, USA
[18] Department of Astrophysical Sciences, Princeton University, 4 Ivy Lane, Princeton, NJ 08540, USA
[19] Center for Computational Astrophysics, Flatiron Institute, 162 Fifth Avenue, New York, NY 10010, USA
[20] University of Toronto Mississauga, 3359 Mississauga Road, Mississauga, ON L5L 1C6, Canada
[21] NASA Ames Research Center, Moffett Field, CA 94035, USA
[22] Department of Physics and Astronomy, University of Kansas, Lawrence, KS 66045, USA
Received 2024 December 20; revised 2025 January 31; accepted 2025 February 26; published 2025 April 1

Abstract

We present the results of the Distant Giants Survey, a 3 yr radial velocity (RV) campaign to search for wide-separation giant planets orbiting Sun-like stars known to host an inner transiting planet. We defined a distant giant (DG) to have $a = 1$–10 au and $M_p \sin i = 70$–$4000\ M_\oplus = 0.2$–$12.5\ M_J$, and required transiting planets to have $a < 1$ au and $R_p = 1$–$4\ R_\oplus$. We assembled our sample of 47 stars using a single selection function and observed each star at monthly intervals to obtain ≈30 RV observations per target. The final catalog includes a total of 12 distant companions: four giant planets detected during our survey, two previously known giant planets, and six objects of uncertain disposition identified through RV/astrometric accelerations. Statistically, half of the uncertain objects are planets and the remainder are stars/brown dwarfs. We calculated target-by-target completeness maps to account for missed planets. We found evidence for a moderate enhancement of DGs in the presence of close-in small planets (CSs), $\mathrm{P(DG|CS)} = 31^{+12}_{-11}\%$, over the field rate of $\mathrm{P(DG)} = 16^{+2}_{-2}\%$. No enhancement is disfavored ($p \sim 8\%$). In contrast to a previous study, we found no evidence that stellar metallicity raises the enhancement of P(DG|CS) over P(DG). We found evidence that DG companions preferentially accompany shorter-period CS planets and have lower eccentricities than randomly selected giant planets. This points toward a nuanced picture of dynamically cool formation in which giants interact with, but do not disrupt, their inner systems.

Unified Astronomy Thesaurus concepts: Exoplanet astronomy (486); Exoplanet detection methods (489); Radial velocity (1332); Bayesian statistics (1900)

1. Introduction

Planets between the size of Earth and Neptune with orbital periods less than 1 yr occur around the majority of Sun-like stars (E. A. Petigura et al. 2018). Meanwhile, giant planets with orbital periods longer than 1 yr occur around 10%–20% of stars (A. Cumming et al. 2008; D. A. Fischer et al. 2014; R. A. Wittenmyer et al. 2020; L. J. Rosenthal et al. 2022). The spread in values arises from different stellar samples along with different definitions of what constitutes a "distant giant planet."

[23] NASA FINESST Fellow.
[24] NASA Postdoctoral Program Fellow.
[25] NSF Graduate Research Fellow.
[26] Kalbfleisch Fellow.
[27] Henry Norris Russell Fellow.
[28] 51 Pegasi b Fellow.

The close-in small-planet (CS) population was compiled primarily using the transit method (Kepler/K2/TESS), while most distant giants (DGs) were discovered with the radial velocity (RV) technique. Historically, transit and RV surveys have targeted nearly disjoint stellar populations (J. T. Wright et al. 2012; J. N. Winn & D. C. Fabrycky 2015), resulting in few systems thoroughly searched for both planet types.

Different planet formation theories disagree on whether the occurrence rates of CS and DG planets should be positively or negatively correlated. In situ models predict that solid rich protoplanetary disks will facilitate the growth of planetary cores both interior and exterior to the ice line, suggesting a positive correlation (e.g., B. M. S. Hansen & N. Murray 2012; E. Chiang & G. Laughlin 2013). By contrast, models that involve significant migration predict that DGs could dynamically perturb the cores of nascent small planets, either barring them from inward migration (A. Izidoro et al. 2015; A. Izidoro & S. N. Raymond 2018) or driving them into their host star (K. Batygin & G. Laughlin 2015; S. Naoz 2016).

Multiple studies have sought to clarify this picture in recent years, by measuring the conditional occurrence of DGs, P(DG|CS), the probability of a system hosting a giant planet given the presence of a CS. Using samples compiled from literature systems with archival RVs, W. Zhu & Y. Wu (2018) and M. L. Bryan et al. (2019) found enhancements of giants in CS-hosting systems over the field rate: P(DG|CS) $\approx$ 30% and P(DG|CS) = 39% $\pm$ 7%, respectively. L. J. Rosenthal et al. (2022) also found an enhancement of P(DG|CS) = 41% $\pm$ 15%, using a uniform sample of legacy RV targets from the California Legacy Survey (CLS; L. J. Rosenthal et al. 2021). In contrast, A. S. Bonomo et al. (2023) found no evidence for a correlation among a sample of 38 Kepler/K2 systems: P(DG|CS) = $9.3^{+7.7}_{-2.9}$%. However, W. Zhu (2024) noted that the average metallicity of the A. S. Bonomo et al. (2023) sample was subsolar and that correcting for this raised the conditional rate to 39^{+12}_{-11}%. The variation among these results highlights the importance of uniform sample selection in statistical analyses. For example, hot-Jupiter occurrence rates measured from transit surveys (~0.6%) differ at the 3σ level from those measured from RV surveys (~0.8%–1.2%), which is likely attributable to the suppression of binary star systems in RV surveys (see J. N. Winn & E. Petigura 2024 and references therein).

The Distant Giants Survey aims to measure P(DG|CS) in a homogeneously compiled sample of Sun-like stars hosting transiting CSs detected by TESS (G. R. Ricker et al. 2015). We introduced the survey and presented the confirmed giant plants in our sample in J. Van Zandt et al. (2023). In this work, we present the completed Distant Giants Survey, including a uniform analysis of the partial orbits in our catalog, as well as our measurement of P(DG|CS). In Section 2, we review our survey's target selection function and observing strategy. We describe our planet detection algorithm in Section 3. We summarize our catalog of full and partial orbit detections in Section 4, and we describe the partial orbits in detail in Section 5. We characterize our survey sensitivity in Section 6, and we measure the conditional occurrence framework in Section 7. We present our results in Section 8 and discuss them in Section 9.

2. Survey Review

The Distant Giants Survey targeted 47 Sun-like ($M_\star$ = 0.5–1.5 $M_\odot$, $T_{\rm eff} < 6250$ K) TESS targets, each hosting at least one transiting planet candidate (N. M. Guerrero et al. 2021), compiled to determine the conditional occurrence rate of long-period gas giants in the presence of inner small planets (J. Van Zandt et al. 2023). We carried out our survey as part of the larger TESS–Keck Survey (TKS), a multi-institutional RV survey of over 100 TESS objects of interest (A. Chontos et al. 2022). We prioritized RV amenability in our sample, selecting stars with low activity ($\log R'_{\rm HK} < -4.7$), low rotational velocity ($v \sin i < 5.0$ km s^{-1}), and high decl. ($\delta > 0°$) to facilitate observations from the Keck and Lick Observatories. We did not require our targets to have prior RV observations, nor did we exclude targets with extant RVs. We required that the transiting companion have $R_p < 10\,R_\oplus$, to include a few sub-Jovian-size planets, but we apply further restrictions on the inner-planet radius in our occurrence calculations (see Section 7). Our final sample exhibits a metallicity consistent with solar (median [Fe/H] = 0.10, $\sigma_{\rm [Fe/H]} = 0.17$ dex). For stars with $T_{\rm eff} > 4800$ K, we report metallicity values calculated using `SpecMatch-Synthetic` (E. A. Petigura 2015), while for stars with $T_{\rm eff} \leqslant 4800$ K, we report metallicities from `SpecMatch-Empirical` (S. W. Yee et al. 2017). We summarize the stellar properties of the targets in the TKS and our sample in Figure 1, and we provide stellar and transiting planet properties in Table B1.

We tailored our observing strategy to detect planets with long periods and large K-amplitudes: we observed each target once per month, primarily using the High Resolution Echelle Spectrometer (HIRES) spectrograph coupled to the Keck I telescope (S. S. Vogt et al. 1994), with supplementary observations for bright targets ($V < 10$) from the Automated Planet Finder (APF)/Levy spectrograph at the Lick Observatory (S. S. Vogt et al. 2014). We used the HIRES exposure meter to integrate to a minimum signal-to-noise ratio of 110 per pixel. We set a goal of 30 total HIRES observations per target over the nominal 3 yr duration of the survey. We obtained median values of 37 RV observations, a 1109 days (3.0 yr) observing baseline, and 1.7 m s^{-1} photon-limited RV uncertainty per target. We add HIRES's 2 m s^{-1} instrumental noise floor (B. J. Fulton 2017) to this last value in quadrature, to obtain 2.6 m s^{-1} total RV uncertainty. We collected a total of 4026 RVs, 1990 of which were taken using Keck/HIRES. We reached at least 25 RVs and at least 1096 days (3.0 yr) baselines for all of our 47 systems. We show our target cadence over the survey duration in Figure 2 and provide a subset of the full RV data set in Table 1.

3. Planet Detection Algorithm

We detected planets using an automated algorithm that we applied uniformly to all RV time series. In broad strokes, our approach follows that of the L. J. Rosenthal et al. (2021) analysis of the CLS. We used the `RVSearch` blind search algorithm to select an RV model by iteratively adding planet signals, then we fit the preferred model to the RV data using `radvel`. However, there are some key differences between our survey and CLS: in the CLS, the targets had more RVs ($N \sim 70$) recorded over longer observing baselines ($t \sim 20$ yr). We therefore tuned the search algorithm to the characteristics of our data set. We summarize our procedure schematically in Figure 3 and provide further details below.

We first established an initial model that included the transiting planet(s), along with their periods P and times of conjunction t_c, which we retrieved from the TESS data

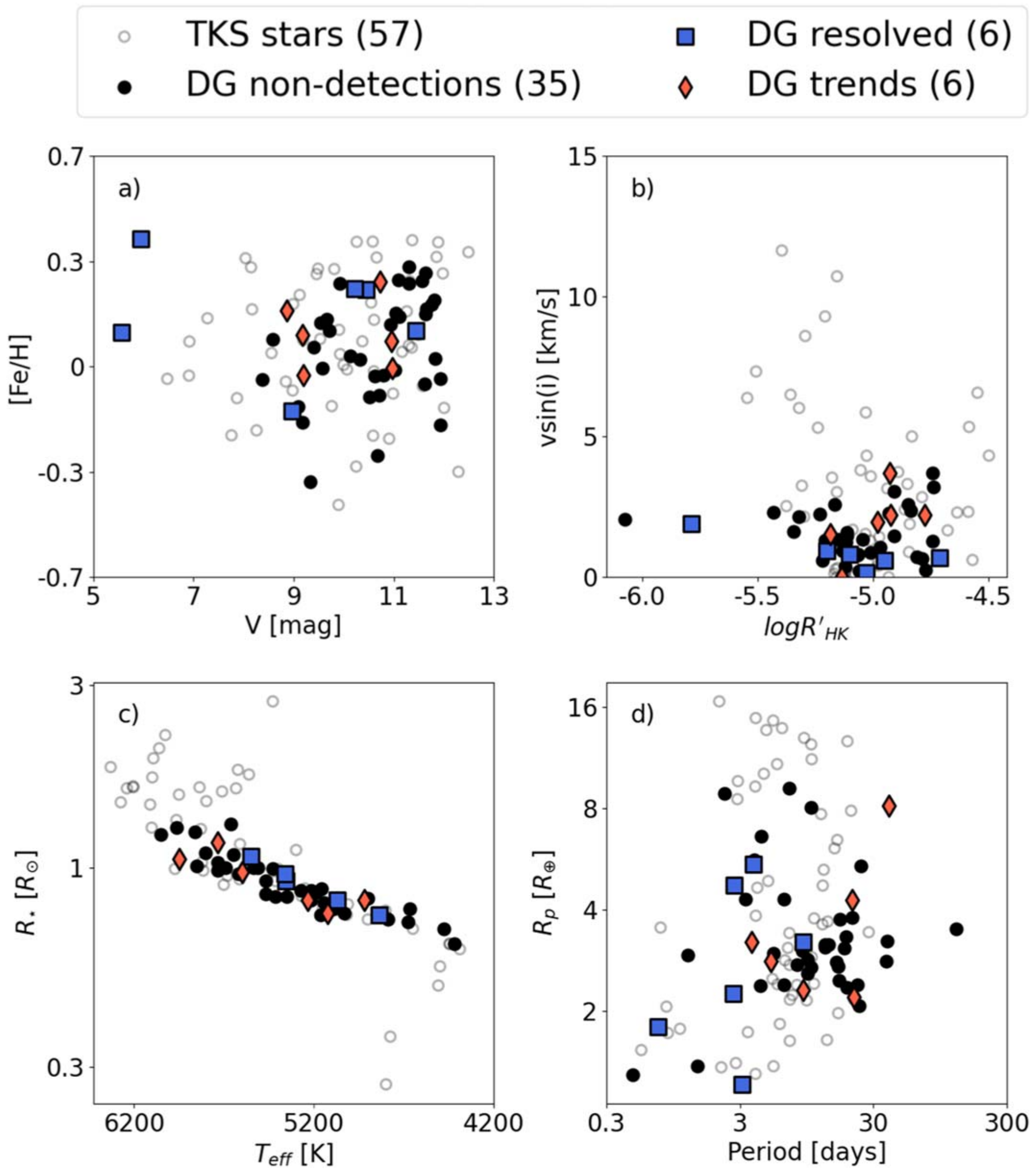

Figure 1. Stellar and transiting planet parameters of the Distant Giants Survey. (a) Metallicity and V-band magnitude of stars with companions detected as resolved orbits (blue squares), stars with companions detected as accelerations (red diamonds), and stars with no detected companions (black circles). The unfilled circles show other systems in the larger TKS. The other panels are same as (a) but for (b) $V \sin i$ and $\log R'_{\rm HK}$, (c) stellar radius and temperature, and (d) transiting planet radius and orbital period. For multitransiting systems, we show the first planet to pass our survey filter (lowest TOI number).

validation reports. We optionally included a linear and/or quadratic term in our model to account for any long-term nonperiodic variability.

Next, we constructed a grid of trial periods. The spacing is such that there is at most a phase slip of 1 radian between the trial periods, to ensure significant peaks are not missed. For each candidate period, we introduced an additional planet to the model, which we will refer to as the "trial planet." With the trial planet's period fixed, we fit the remaining orbital parameters—time of periastron t_p, eccentricity e, argument of periastron ω, and RV semi-amplitude K. If a trend was included based on the prior step, we allowed its parameters to vary as well. During the fitting, we held the parameters of all other planets fixed. We calculated the change in the Bayesian Information Criterion (ΔBIC; G. Schwarz 1978) between each model and a model without the added planet. We repeated this step for all trial periods to produce a ΔBIC periodogram.

In principle, we may adopt any significance threshold to accept or reject periodic signals, provided that it is used in both the initial search and the completeness correction (described in Section 6). We identified $\Delta\text{BIC} > 30$ as a threshold that produced relatively few false-positive and false-negative detections across our sample. If the maximum ΔBIC value did not exceed 30, we removed the trial planet from the model, designated the current model as preferred, and terminated the search. If the maximum ΔBIC exceeded 30, we refined the fit using a finer period search and performed a final comparison to select a trend or a planetary model. To do this, we generated three copies of the orbit model: (1) trial planet and no trend; (2) no trial planet and a trend; and (3) both trial planet and trend. From these, we selected the model with the highest ΔBIC.

If our three-way model comparison favored a trend only, we designated the current model as preferred. Otherwise, we added another planet to our model and repeated the search until one of

Figure 2. RV observations of the Distant Giants Survey. In total, we collected 1990 RVs from Keck/HIRES (red squares) and 2036 observations from APF/Levy (gray circles) between 2020 August 1 and 2024 January 31. Note that a few targets had prior RVs that are not shown. TOI identifiers are shown in the left margin, ordered by R.A. Each year label on the *x*-axis marks February 1, the first day of the "A" observing semester. The typical target in our survey is not accessible from Keck for about three months per year, resulting in the diagonal cadence gaps. The eruption of Mauna Loa in 2022 November, as well as unrelated damage to the lower shutter of the Keck I dome between 2022 November and 2023 May, resulted in a substantial decrease in observation cadence for targets between R.A. $\sim$ 16 and 22 hr, which did not reach elevations $>40^\circ$ during this period.

Table 1
DG RVs

TOI	TKS Name	BJD	RV ($\mathrm{m\ s^{-1}}$)	RV Error ($\mathrm{m\ s^{-1}}$)	Instrument
TOI-465	WASP156	2.459071e+06	−18.054364	1.564020	hires_j
TOI-465	WASP156	2.459093e+06	1.107389	1.559804	hires_j
TOI-465	WASP156	2.459143e+06	−0.437076	1.581019	hires_j
TOI-465	WASP156	2.459182e+06	−12.919443	1.729959	hires_j
TOI-465	WASP156	2.459239e+06	5.979829	2.182647	hires_j
TOI-465	WASP156	2.459269e+06	18.029111	1.558576	hires_j
TOI-465	WASP156	2.459396e+06	11.567155	1.714726	hires_j
TOI-465	WASP156	2.459445e+06	21.068103	1.478714	hires_j
TOI-465	WASP156	2.459477e+06	1.831015	1.563436	hires_j

Note. A subset of the RV measurements used in our analysis. All measurements were collected between 2020 August 1 and 2024 January 31 using the Keck/HIRES and APF/Levy spectrometers. We provide the full set of 4026 RVs online.

the termination conditions was met. As an additional termination condition, we set a maximum of eight planets on each system's model, though in practice never found evidence for more than two. After determining our final preferred model, we derived credible orbital solutions by sampling our posterior probability with `emcee` (D. Foreman-Mackey et al. 2013).

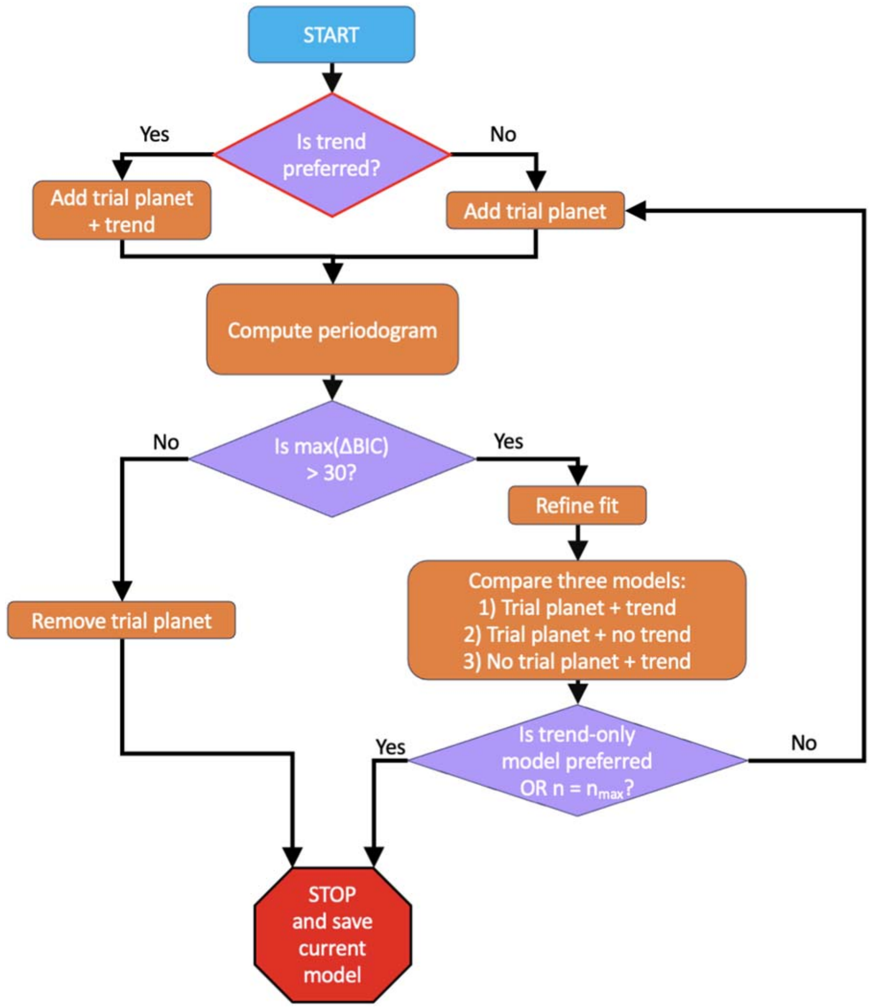

Figure 3. Flow diagram of our planet detection algorithm. We used the same algorithm for detecting planets (Section 4) and for computing the completeness (Section 6). We began by initializing an orbital model with the RV data and the ephemerides of any known transiting planets. We then determined whether the data supported the inclusion of a trend—that is, if a trend model was favored over a flat model by ΔBIC > 5—after which we added a new planet to the model. We computed (ΔBIC) between the starting model and a model with a trial planet over a dense grid of trial periods. If the maximum ΔBIC exceeded 30, we performed a final model comparison test to select a model with a planet, a trend, or both. We iteratively added planets to the model in this way until no more were found. For the injection/recovery experiments described in Section 6, we began with the final model from Section 4, to retain any planets found during the initial search. We then injected a synthetic planetary signal into the data and began the recovery at the trend test step (outlined in red). When the search terminated, we checked whether the injected signal was recovered, either as a planet or as a trend, and recorded the result.

4. Planet Catalog

4.1. Six Companions with Resolved Orbits

We identified six giant planets with $P \lesssim t_{\rm base}$ where we could fully resolve the orbits and measure planetary parameters with small fractional uncertainties. Two such planets—HD 219134 g (S. S. Vogt et al. 2015) and HD 75732 d (D. A. Fischer et al. 2008)—were known prior to the start of our survey. We announced the discovery of two more—TOI-1669 b and TOI-1694 c—in J. Van Zandt et al. (2023) and confirmed the mass of HD 191939 f in J. Lubin et al. (2024). E. Knudstrup et al. (2023) independently resolved TOI-1288 c for a total of six giants. We display the masses and periods of these giants and their inner companions in Figure 4 and Table 2.

4.2. Six Companions with Partial Orbits

We detected six massive companions as long-term linear and/or quadratic RV trends and list them in Table 3. We noted that multiple trends with 3σ significance manifested in our sample, only to be ruled out by subsequent RV measurements. We therefore adopted a trend threshold of 4σ, to exclude these signals while retaining as many true trends as possible. The masses and orbital periods of such objects have large uncertainties; often the RVs alone are insufficient to determine whether the object is a planet, brown dwarf, or star. We compute the relative probability of each scenario in Section 5, incorporating astrometric and imaging constraints where available. In Figure 5, we show the planet masses and separations for each system in our survey and indicate the systems in which we detected a trend.

4.3. Treatment of Presurvey Data

A handful of our targets' data sets significantly exceed our 3 yr, 30-observation criteria. For example, HD 219134 and HD 75732 each have >600 observations over ~30 yr. For such data sets, it is possible to detect many planets. We found that our detection pipeline, which was tuned for $N \sim 30$ observations and $t_{\rm base} \sim 3$ yr, struggled to identify the correct orbital parameters of

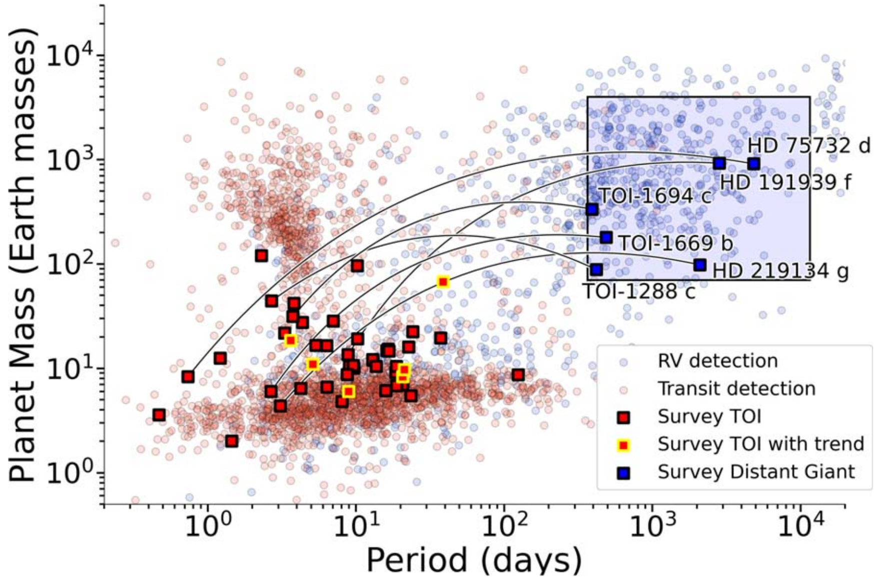

Figure 4. CSs and their DG companions. Masses and periods of exoplanets from our survey (bold squares) and the NEA (faded circles) are shown for context. The red/blue points indicate planets discovered using the transit/RV method. The red squares show the true masses of transiting planets in the Distant Giants Survey measured by RVs (A. S. Polanski et al. 2024), while the blue squares show minimum mass measurements ($M \sin i$). For systems with multiple transiting planets, we show the parameters of the transiting planet with the lowest TOI designation that passed our filters. The red squares with yellow borders indicate systems in which we detected a linear/quadratic trend. The giant planets in our sample are connected to the inner planet in their system by a black line. The box corresponds to our nominal definition of a DG.

Table 2
Resolved DG Planet Properties

TOI	TKS Name	Transiting Planet Period (days)	Transiting Planet Radius ($R_\oplus$)	Transiting Planet Mass ($M_\oplus$)	Giant Planet Period (days)	Giant Planet Separation (au)	Giant Planet $M \sin i$ (M_J)	
1288	T001288	2.7	5.24 ± 0.09	42 ± 3	443^{+11}_{-13}	1.1 ± 0.4	0.26 ± 0.02	1
1339	191939	8.9	3.39 ± 0.07	10.4 ± 0.9	2744 ± 146	3.6 ± 0.2	2.7 ± 0.3	2
1469	219134	3.1	1.3 ± 0.6	4.5 ± 0.5	2101 ± 3	3.06 ± 0.04	0.31 ± 0.01	3, 4
1669	T001669	2.7	2.4 ± 0.2	5 ± 3	502 ± 16	1.13 ± 0.03	0.57 ± 0.07	5
1694	T001694	3.8	5.4 ± 0.2	26 ± 2	389 ± 4	0.98 ± 0.02	1.05 ± 0.05	5
1773	75732	0.7	2.0 ± 0.3	8.3 ± 0.3	5285 ± 5	5.61 ± 0.09	3.84 ± 0.08	4, 6

Note. The rightmost column gives the reference(s) for giant-planet mass and period, as well as the transiting planet mass, if available. We list our own fitted giant-planet separations. For TOI-1288, the reference is for all parameters of both planets. We cite transiting planet parameters for HD 191939 from J. Lubin et al. (2022). We cite transiting planet parameters for the remaining systems from the TESS Data Validation Reports. Typical transiting planet period uncertainties are of order 10^{-4}–10^{-5} days. We include HD 191939, HD 219134, and HD 75732 in this table because we detected them in our full RV data sets. However, we treat these signals as trends in our homogeneous statistical analysis.

References. (1) E. Knudstrup et al. (2023); (2) J. Lubin et al. (2024); (3) S. S. Vogt et al. (2015); (4) L. J. Rosenthal et al. (2021); (5) J. Van Zandt et al. (2023); and (6) R. I. Dawson & D. C. Fabrycky (2010).

the smaller planets in these systems. We opted for a simple scheme, by setting a maximum observing baseline of 4 yr, which truncated the data sets of four systems: HD 207897, HD 191939, HD 219134, and HD 75732. The last three of these each host a DG with $P > 5$ yr, which presented as trends in the truncated data. We treated these signals as trends for our trend analysis (Section 5) and occurrence calculations (Section 7), but recognized their planetary nature in our analysis of correlations between DGs and inner-small-planet properties (Section 8). HD 219134 and HD 75732 each have many 4 yr windows that we could have selected for our analysis. We conducted our occurrence calculation multiple times, using different observing windows and therefore sampling different phases of the giant planet in each system, to verify that our results were not sensitive to our choice of observing window.

5. Trend Analysis

5.1. Ethraid

We characterized companions detected as trends using `ethraid` (J. Van Zandt & E. Petigura 2024a). This code determines the masses and orbital periods that are consistent with a measured RV trend, imaging constraints, and/or astrometric accelerations through importance sampling.

We assumed that the measured signal originated from a single object (as opposed to multiple bodies or stellar activity). We also assumed that its semimajor axis is between 3 and 64 au; smaller orbits would be resolved as Keplerians and objects with larger orbits would have such high masses that they would be easily detected as stars. We considered companions between 0.1 and 1000 M_J, covering planets, brown

Table 3
DG Trend Data

TOI	TKS Name	$\dot{\gamma}$ (m s^{-1} yr^{-1})	$\ddot{\gamma}$ (m s^{-1} yr^{-2})	$\Delta\mu$ (mas yr^{-1})	Direct Imaging?	P(planet)	P(BD)	P(star)
1174	T001174	-27.0 ± 3.7	14.3 ± 2.1	⋯	True	0.53	0.22	0.26
1339	191939	26.9 ± 0.5	-9.9 ± 0.5	0.13 ± 0.03	True	0.98	0.02	0.00
1438	T001438	10.9 ± 1.4	-13.5 ± 1.7	⋯	True	0.79	0.08	0.12
1469	219134	-4.4 ± 0.3	0.0 ± 0.0	0.15 ± 0.06	True	1.00	0.00	0.00
1471	12572	-22.0 ± 0.4	-0.5 ± 0.5	0.07 ± 0.05	True	0.61	0.08	0.31
1742	156141	13.1 ± 0.5	-6.4 ± 0.5	⋯	True	0.78	0.15	0.08
1773	75732	-68.6 ± 12.5	6.8 ± 1.0	0.07 ± 0.06	False	0.91	0.03	0.07
1797	93963	-9.4 ± 1.8	-12.7 ± 1.8	⋯	True	0.81	0.07	0.12
1823	TIC142381532	-8.6 ± 2.1	0.5 ± 0.9	⋯	True	0.32	0.31	0.38
Total						6.73	0.96	1.34

Note. RV, astrometric, and imaging information for the nine trend systems in our sample. We include HD 191939, HD 219134, and HD 75732 in this table, despite knowing that their trends are planetary in origin, because we treated their signals as trends in our statistical analysis. The three columns to the right give the probability of the measured signal in each system originating from a planetary, brown dwarf, or stellar companion between 3 and 64 au. We derived these probabilities by integrating the posterior distributions we calculated using `ethraid` over the appropriate mass interval. Summing the probabilities for each object type suggests that these nine systems host five to six planets, two to three brown dwarfs, and ∼one stellar companion.

dwarfs, and low-mass stars. We adopted an informative *M–a* prior, which we expand upon in Section 5.2

We included astrometric constraints from the Hipparcos−Gaia Catalog of Accelerations (HGCA; T. D. Brandt 2021) and imaging constraints from A. S. Polanski et al. (2024). The joint *M–a* constraints for these objects are shown in Appendix A, along with notes on each system. For each system, we collected the posterior samples output by `ethraid` and integrated the distribution over three mass intervals: $M < 13\,M_J$, $13\,M_J < M < 80\,M_J$, and $80\,M_J < M$. We report these fractions in Table 3 as the probability that the companion is a planet, brown dwarf, or star, respectively.

5.2. Mass–Separation Prior

We implemented a prior on mass and separation to reflect the intrinsic prevalence of companions with different properties. We derived this prior distribution based on the occurrence rates of substellar (CLS; L. J. Rosenthal et al. 2021) and stellar (D. Raghavan et al. 2010) companions to Sun-like stars.

We chose to define this prior over the interval 0.03–64 au, 0.05–1000 M_J, extending to smaller masses and separations than our trend analysis required, both because the CLS has high sensitivity and many detections in this regime (see Figure 6) and to examine features of planet and brown dwarf occurrence as a function of separation (see Section 9.4). We calculated the survey completeness in this domain using the ensemble of injection/recovery experiments published by L. J. Rosenthal et al. (2021).[29] Following previous occurrence studies (see J. N. Winn & E. Petigura 2024 for a review), we divided this region into two-dimensional intervals uniform in logarithmic space. We used five intervals in mass and five intervals in semimajor axis, giving 25 cells. Our mass bins approximately correspond to sub-Jupiters (0.05–0.3 M_J), Jupiter analogs (0.3–3 M_J), super-Jupiters (3–13 M_J), brown dwarfs (13–80 M_J), and stars (80–1000 M_J). We chose our semimajor-axis bounds to approximate log-uniform spacing between 0.03 and 64 au. We employed the Poisson occurrence method of Section 7.2 to calculate the occurrence rate in each cell.

[29] Accessible at https://github.com/leerosenthalj/CLSI/tree/master.

For our stellar prior, we used the stellar period distribution of D. Raghavan et al. (2010). They fit a normal distribution to a log-period histogram of 259 stellar companions detected among a sample of 454 Sun-like stars, finding that $\log P \sim \mathcal{N}(5.03, 2.28)$. We integrated this distribution to estimate the number of companions in each of our five semimajor-axis intervals. We then applied the same occurrence model to these cells, approximating 100% completeness. We illustrate our mass–separation prior in Figure 6.

6. Survey Sensitivity

6.1. Distant Giants Survey

While we designed the Distant Giants Survey to yield a high uniformity in sensitivity to DGs, each star has differences in RV noise properties, observational sampling, and other properties. We evaluated our sensitivity to both resolved and partial orbits on a star-by-star basis, using an injection/recovery scheme.

We began with the system's preferred orbital model (see Section 3), subtracted any fitted trend/curvature from the data, and injected a synthetic planetary model. We generated these planets according to the following distributions: $\log P \sim \mathcal{U}(\log P_{\min}, \log P_{\max})$, $\log K \sim \mathcal{U}(\log K_{\min}, \log K_{\max})$, $e \sim \mathcal{B}(0.867, 3.03)$, $t_p \sim \mathcal{U}(0, P)$, and $\omega \sim \mathcal{U}(0, 2\pi)$. Here, $P_{\min}, P_{\max} = (250\text{ days}, 15{,}000\text{ days})$, $K_{\min}, K_{\max} = (2\text{ m s}^{-1}, 300\text{ m s}^{-1})$, and $\mathcal{B}(0.867, 3.03)$ is the beta distribution fit by D. M. Kipping (2013), which we chose to match L. J. Rosenthal et al. (2021; see Section 6.2). Figure 7 shows the suite of experiments for TOI-1173 as an example. We permitted our algorithm to identify at most one additional planet via the same blind search described in Section 3 and in Figure 3, beginning by testing for a trend.

When the search terminated, we recorded any signals recovered during the search. We considered a planet successfully recovered if P, t_p, and K matched the injected values to 25% or better. We considered a recovered trend significant if the fitted value corresponded to $\geqslant 8\text{ m s}^{-1}$ RV variation (i.e., three times the typical RV measurement error) over a 3 yr period. This threshold excluded low-significance trends in an analogous way to our 4σ trend threshold for our real catalog.

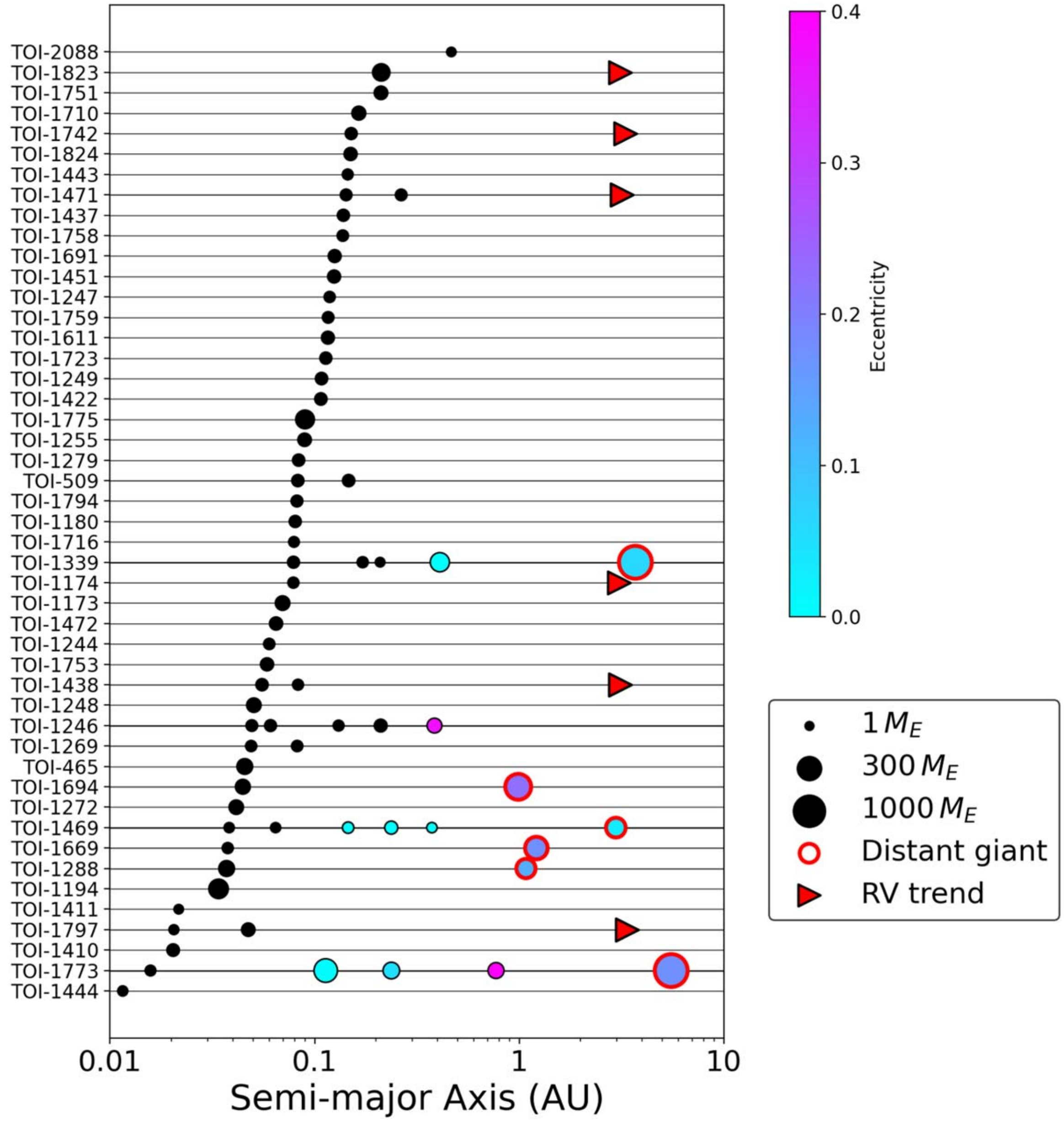

Figure 5. Masses and orbital spacings of the planets in each system in our survey. The systems are ordered according to the semimajor axis of the innermost transiting planet. Transiting planets are shown with black markers, and nontransiting planets are colored according to their eccentricity. The marker sizes are proportional to the square root of the planet true mass (for transiting planets) or minimum mass (for nontransiting planets). We use red borders to indicate the planets that meet our definition of a DG. For systems with RV trends, we place a red triangle at a separation corresponding to 6 yr, the approximate maximum period for which we could resolve a Keplerian orbit. Based on Figure 4 of L. M. Weiss et al. (2024).

We computed completeness maps in a–$M \sin i$ space for each target by performing a moving average over the set of successful and unsuccessful detections (see Figure 7 for an example). The survey sensitivity is the average of all individual maps (see the bottom row of Figure 7). As a point of reference, our sensitivity to Jupiter-mass planets as resolved orbits is nearly 100% at 1 au and declines to 60% near 2 au (roughly the average baseline). Planets three times the mass of Jupiter are recovered as trends with 60% completeness between 3 and 10 au.

6.2. CLS

To calculate the field occurrence rate of DGs, P(DG), we averaged together the 719 target-by-target completeness maps computed by L. J. Rosenthal et al. (2021) for the CLS sample. Their sensitivity is superior to ours, due to their larger RV data sets and longer target baselines. For example, they maintain $\geqslant$50% sensitivity to 1 M_J objects out to 6 au (see Figure 8), whereas our sensitivity to Jupiter analogs drops precipitously beyond 2 au.

A direct comparison of the DG conditional occurrence to the CLS field occurrence makes the implicit assumption that the two samples have the same inclination distribution. However, if multiplanet systems inside/outside 1 au are highly aligned, our selection of systems with transiting planets will favor DG planets with edge-on orbits. All else being equal, we would expect increased sensitivity at a given mass in the DG sample, since edge-on planets are easier to detect.

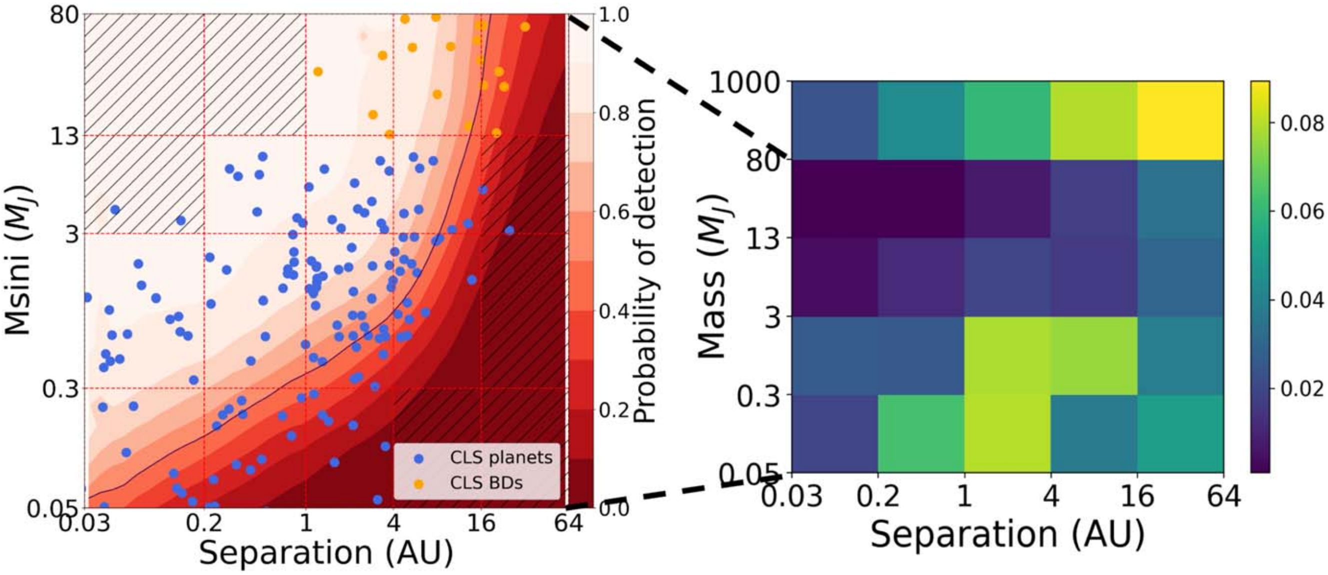

Figure 6. Mass–separation prior informed by the L. J. Rosenthal et al. (2021) and D. Raghavan et al. (2010) surveys. Left: minimum masses and orbital separations of the CLS (L. J. Rosenthal et al. 2021) sample of planets (blue points) and brown dwarfs (orange points). We also show the survey-averaged completeness map (red contours), emphasizing the 50% contour with a black line. We compute the companion occurrence in the cells defined by the red dashed lines. The hatch marks show cells containing fewer than three objects, giving rise to highly uncertain occurrence rates. However, inspection of the RV constraints in Appendix A shows negligible overlap with these regions, so they do not affect our overall results. Right: the domain of M and a we explore in our companion search. Each M–a subdomain is colored with the number of objects per star and serves as our joint M–a prior described in Section 5.2. The highest-mass bins are based on the D. Raghavan et al. (2010) rates.

In the limiting case where all CS+DG systems are perfectly aligned (i.e., $\sin i = 1$), the completeness maps shown in Figure 7 should be interpreted as M–a (as opposed to $M \sin i$–a). On the other hand, if all systems have random orientations, then the maps are on equal footing with those of the CLS sample.

We modeled both extremes by recomputing the CLS completeness in the following manner: for each injected orbit, we drew 10 inclinations from a distribution uniform in $\cos i$. We then generated 10 realizations of the true mass of the injected companion by dividing $M \sin i$ by $\sin i$ for each of the inclination draws. We maintained each injection's status as a successful/unsuccessful recovery during this process. We then computed the survey-averaged completeness of the CLS in M–a (as opposed to $M \sin i$–a). The difference between the corrected and uncorrected maps is minor: at 3 au, the CLS sensitivity to $M \sin i = 1\,M_J$ is 60%, while the sensitivity to $M = 1\ M_J$ is 50%. We show both extremes in Figure 8.

The average completeness of the CLS survey to minimum masses within our nominal DG domain is 59%, while the sensitivity to true masses in the same interval is 52%. This change produces a 1σ (2%) difference in our inferred field occurrence rate P(DG).

7. Computing Planet Occurrence

7.1. Definitions

In this work, we define a "close-in" planet to have $a < 1$ au and a distant planet to have $a = 1$–10 au. We define a "small" planet to have $R_p = 1$–$4\,R_\oplus$ for CSs and a "giant" planet to have $M = 70$–$4000\,M_\oplus$ (0.22–12.6 M_J). We also consider modified boundaries when making direct comparisons to previous studies.

7.2. Occurrence Model

Our goal is to measure both the conditional occurrence of giant planets in systems with small planets P(DG|CS) *and* the field occurrence rate of giant planets P(DG) and compare the two rates. For both rates, we are considering the number of planets per star.

Following the prescription in L. J. Rosenthal et al. (2022), we modeled our observed planet catalog as a realization of a censored Poisson process. The process is censored because some planets are missed in regions of imperfect survey completeness ($Q(a, M) < 1$). Our task is to infer the parameters, $\boldsymbol{\theta}$, of the occurrence-rate density function $\lambda(a, M|\boldsymbol{\theta})$, where the latter is defined as the number of planets per star per $\log a$–$\log M$ interval. We model λ as log-uniform over the DG domain; $\boldsymbol{\theta}$ is thus a single number.

The appropriate likelihood has been described previously (e.g., J. G. Rogers & J. E. Owen 2021) and is

$$P(\{\boldsymbol{\omega}\}, N_p|\boldsymbol{\theta}) = \frac{e^{-\Lambda}\Lambda^{N_p}}{N_p!} \prod_{k=1}^{N_p} \frac{Q(\boldsymbol{\omega}_k)\lambda(\boldsymbol{\omega}_k|\boldsymbol{\theta})}{\Lambda}. \tag{1}$$

Here, N_p is the number of observed planets, $\boldsymbol{\omega}_k$ is the (a, M) tuple for the kth planet, and Λ—the "intensity parameter"—is

$$\Lambda = N_\star \int Q(\boldsymbol{\omega}_k)\lambda(\boldsymbol{\omega}_k|\boldsymbol{\theta})\, d\log(a) d\log(M), \tag{2}$$

where $N_\star$ is the number of host stars in our sample. Conceptually, the likelihood in Equation (1) can be understood as the product of two terms: the term before the product operator is the probability of observing N planets regardless of their parameters, and the second is the probability of observing those planets with their specific a and M values.

Since companions are either detected as trends or resolved orbits, we construct separate likelihoods for each and multiply their results:

$$P(\{\boldsymbol{\omega}_{\rm pl}, \boldsymbol{\omega}_{\rm tr}\}, N_{\rm pl}, N_{\rm tr}|\boldsymbol{\theta}) = P(\{\boldsymbol{\omega}_{\rm pl}\}, N_{\rm pl}|\boldsymbol{\theta}) \cdot P(\{\boldsymbol{\omega}_{\rm tr}\}, N_{\rm tr}|\boldsymbol{\theta}). \tag{3}$$

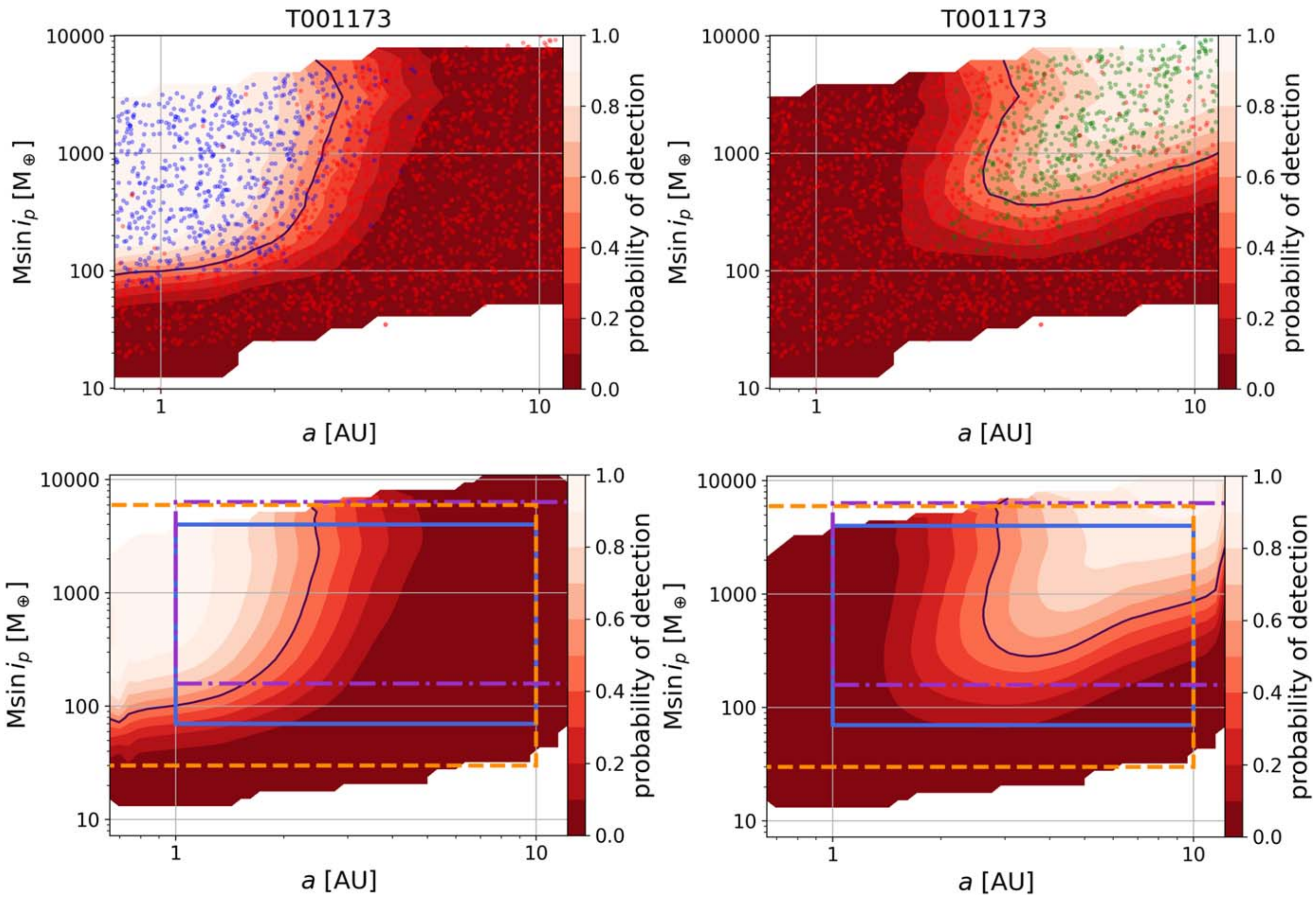

Figure 7. Side-by-side comparison of injection/recovery results and calculated completeness to resolved orbits (left) and trends (right). We tracked whether our automated search algorithm recovered injected RV signals successfully (blue/green points for resolved orbits/trends) or unsuccessfully (red points). From this collection of recoveries, we calculated a sensitivity map, with the contour lines marking completeness deciles and the black contour denoting the 50% completeness boundary. We injected 2000 signals for each system. Top row: completeness for a typical system in our survey (TOI-1173: 3.9 yr baseline, 27 observations). Bottom row: average completeness of the 47 targets in our survey, with the blue boxes indicating our nominal definition of a DG. Our average sensitivity in this interval is 30% for resolved orbits and 35% for trends. The orange and purple dashed boxes indicate the giant-planet definitions used by L. J. Rosenthal et al. (2022) and M. L. Bryan et al. (2019), respectively. Our survey had 32% (27%) sensitivity to resolved orbits (trends) using the L. J. Rosenthal et al. (2022) definition and 30% (43%) sensitivity using that of M. L. Bryan et al. (2019). Note that we treated resolved orbits and trends as distinct detection classes, meaning that an orbit recovered as a trend was considered an unsuccessful recovery in the resolved recovery map and vice versa.

Here, the subscripts "pl" and "tr" refer to the resolved and trend subsamples, respectively.

We capture catalog uncertainties by sampling many catalog realizations from our full set of posteriors, where each realization comprises one sample from each of the 12 posteriors (three resolved orbits and nine trends). We discard any of the samples that fall outside of our occurrence domain and derive the posterior surface using Equation (3). We average together many such distributions to obtain a robust estimate of the occurrence-rate density.

7.3. Occurrence Computation

We used this occurrence methodology to calculate P(DG|CS). We first collected the posterior distributions for all systems hosting a resolved DG or a trend. For the resolved planet posteriors, we used Gaussian distributions defined by the planet parameters in Table 2. For the trends, we used posterior distributions produced by `ethraid` (see Appendix A). We drew one sample from each posterior distribution, kept only the samples that satisfied our DG definition, and used Equation (3) to calculate the planet occurrence with that realization of our catalog. We repeated this procedure 500 times and averaged the resulting planet occurrence estimates to account for our uncertainties.

8. Results

8.1. DGs May Be Enhanced in the Presence of CSs

Using the procedure described in Section 7, we found a conditional occurrence rate of $\mathrm{P(DG|CS)} = 31^{+12}_{-11}\%$. We then calculated P(DG) to be between $16^{+2}_{-2}\%$ (not inclination-corrected) and $18^{+2}_{-2}\%$ (inclination-corrected) using the sample of L. J. Rosenthal et al. (2021). The true field rate is likely intermediate between these two extremes. Our results suggest with 1σ confidence that P(DG|CS) is enhanced over P(DG) by a factor of $\lesssim 2$.

To quantify the significance of the enhancement, we randomly drew 10^4 values from the P(DG|CS) and P(DG) posteriors and found P(DG|CS) > P(DG) among 92% of the draws. An analogous experiment with the inclination-corrected P(DG) returned 90%. We therefore conclude that P(DG|CS) is enhanced over P(DG) with $\geqslant$90% confidence and that inclination disparities caused by our transit-hosting sample do not significantly affect this result. We summarize our results in

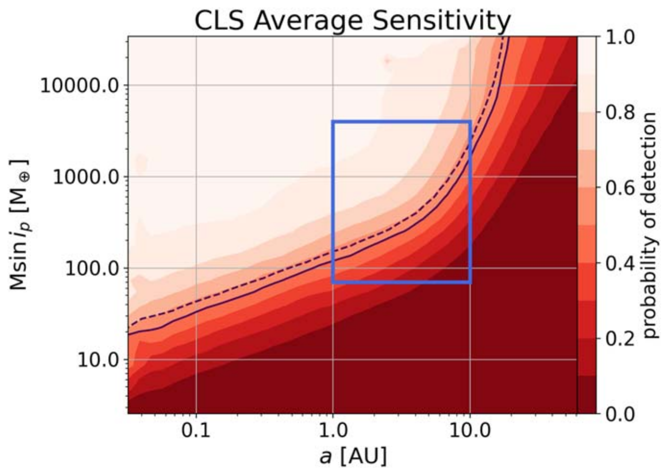

Figure 8. Average sensitivity to companions as a function of minimum mass and separation for the CLS. The shaded regions show domains of constant detection probability, and the solid black contour shows the 50% detection probability boundary. We recalculated this map after adjusting for inclination effects to determine the CLS sensitivity to true mass (see Section 6.2). We show the 50% boundary of the adjusted map as a dashed black line. We use a blue rectangle to show our nominal definition of a DG (a = 1–10, M = 70–4000$M_\oplus$). The average CLS sensitivity to minimum/true masses within this domain is 59%/52%.

Figure 9 and report our calculated occurrence rates under our nominal planet definitions in Table 4.

We repeated our analysis with planet definitions that more closely match those of L. J. Rosenthal et al. (2022; hereafter, R22) and M. L. Bryan et al. (2019; hereafter, B19; see the bottom row of Figure 7). R22 adopted the following definitions: DG–$a = 0.23$–10 au, $M_p \sin i$ = 30–6000 $M_\oplus$; CS–$a = 0.023$–1 au, and $M_p \sin i = 2$–30 $M_\oplus$. The 30 $M_\oplus$ boundary corresponds to $R_p \sim 6\,R_\oplus$ (J. Chen & D. Kipping 2017). With this definition, we found P(DG|CS) = 34^{+17}_{-13}% and P(DG) = 20^{+2}_{-2}%, as well as a 95% probability that P(DG|CS) > P(DG). Our conditional rate is also consistent with R22's finding of P(DG|CS) = 41^{+15}_{-13}% using a different sample, though our field rate is 1σ higher than their value of P(DG) = $17.6^{+2.4}_{-1.9}$%, likely owing to our exclusion of M dwarfs from the CLS sample.

B19 required that a = 1–20 au, $M_p \sin i = 0.5 - 20\,M_{\rm J}$ for DGs, and R_p = 1–4$R_\oplus$ for CSs. Under this definition, we found P(DG|CS) = 24^{+13}_{-10}%, lower than their quoted rate of 39% ± 7% and marginally enhanced over the field rate of P(DG) = 16^{+2}_{-2}%. We expect that this disagreement is due to differences in both our stellar samples and completeness correction procedures. Using the R22 and B19 definitions, we found evidence for an enhancement of P(DG|CS) at 95% and 78% confidence, respectively (see Figure 9). We list the results of these tests in Table 4. We did not perform $\sin i$ corrections when replicating the field-rate calculations of R22 and B19, because these studies did not select purely for transiting inner planets in their stellar samples.

8.2. No Strong Evidence That High-metallicity Systems Exhibit a Greater Enhancement of DGs

W. Zhu (2024) and M. L. Bryan & E. J. Lee (2024) reported an enhancement of DGs in the presence of CSs specifically in metal-rich ([Fe/H] > 0) systems, beyond the enhancement expected from the established occurrence–metallicity relation (D. A. Fischer & J. Valenti 2005). J. Van Zandt & E. A. Petigura (2024b) tested this claim by repeating the analysis of M. L. Bryan & E. J. Lee (2024) but using a single sample to measure both the field and conditional occurrence in metal-rich systems. They did not find evidence that the enhancement was specific to metal-rich systems.

We tested the effect of metallicity on giant-companion occurrence in the DG sample by repeating the analysis of Section 7 with only metal-rich systems. Of the 47 systems in our sample, 19 have supersolar metallicity and host a CS under 4 $R_\oplus$. This subsample includes one of the three systems with a resolved giant with P < 5 yr (TOI-1669), two of the three systems with a resolved giant with P > 5 yr (HD 219134 and HD 75732), and three of the six trend systems (TOI-1438, HD 156141, and HD 93963). We calculated a metal-rich conditional occurrence rate of P(DG|CS, [Fe/H]>0) = 44^{+22}_{-18}%. We applied the same filters to the CLS sample and found a metal-rich field rate of P(DG|[Fe/H] > 0) = 23^{+3}_{-3}%, yielding a probability of 89% that P(DG|CS, [Fe/H] > 0) is enhanced over P(DG|[Fe/H]>0), similar to our results using the non-metal-rich sample. We conclude that there is not strong evidence that metal-rich systems exhibit a greater enhancement of the conditional DG occurrence rate over the field rate than field stars do.

We also calculated the occurrence using the 16 metal-poor systems in our sample that host a CS under 4 $R_\oplus$. We found P(DG|CS, [Fe/H] < 0) = 20^{+19}_{-12}%, against a field rate of P(DG|[Fe/H] < 0) = 6% ± 2%, giving an 89% probability of enhancement. Our conditional rate is based on two systems, HD 191939 ([Fe/H] = −0.15) and TOI-1174 ([Fe/H] = −0.004), making it highly uncertain. Additionally, TOI-1174's metallicity is consistent with solar. Excluding this system from the calculation gives P(DG|[Fe/H] < 0) = 16^{+15}_{-10}% (84% enhancement probability). Both of these cases show occurrence rates consistent with an enhancement, though we caution that they are derived using small samples. Despite the large uncertainties, our results in analyzing the metal-rich, metal-poor, and full samples indicate that metallicity does not exert a strong influence on the relative enhancement of giants. Rather, both the conditional and field occurrence rates rise with metallicity, maintaining an approximately fixed ratio.

8.3. Inner Companions to Resolved Giants May Be Preferentially Closer In

Inspection of Figures 1, 4, and 5 shows that CSs with resolved DGs have shorter periods on average than the parent sample. We conducted a two-sample Kolmogorov–Smirnov test (F. J. Massey 1951) to determine whether the separations of the close-in companions in the six systems hosting a resolved giant were drawn from the same distribution as the separations of the close-in companions in the 35 systems with neither a resolved giant nor a trend. In systems with multiple transiting planets, we used the separation of the first TOI detected in the system. We found a p-value of 0.006, meaning that under the assumption that the two populations are drawn from the same distribution, we would expect discrepancies greater than or equal to those observed to occur with 0.6% probability. We repeated this test using only the subset of our targets with transiting planet radii <4 $R_\oplus$, finding p = 0.015. Our findings suggest that outer giants tend to have lower-separation inner companions and that this trend may be slightly weaker for inner companions with smaller radii. We note that the transiting companion with the shortest period, HD 75732 e, is also accompanied by a 14 days warm Jupiter, which likely had a more significant dynamical impact on it than the DG in this

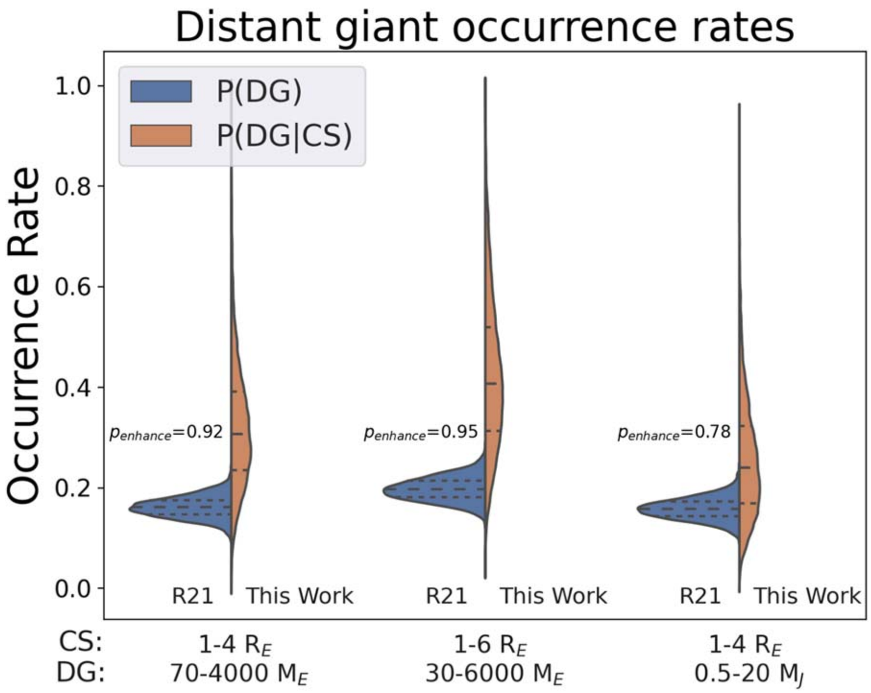

Figure 9. Measurements of the field (blue) and conditional (orange) occurrence rates of DGs under different planet definitions. The black lines show distribution quartiles. The distributions to the left show occurrence rates for our nominal definitions: $a = 1$–10 au, $M_p \sin i = 70$–4000 $M_\oplus$ for DGs and $a > 1$ au, $R_p = 1$–4 $R_\oplus$ for CSs. The distributions in the center and right show occurrence rates for planet definitions matching those of L. J. Rosenthal et al. (2022) and M. L. Bryan et al. (2019), respectively. We annotate each distribution with the probability that the conditional rate is enhanced over the field rate.

Table 4
DG Occurrence Rates

DG Mass Limits ($M_\oplus$)	$N_\star$ (CLS)	N_{DG} (CLS)	P(DG)	CS Radius Limits ($R_\oplus$)	$N_{transiting}$	$N_{resolved}$	N_{trend}	P(DG|CS)
70–4000	598	55	16^{+2}_{-2}%	1–4	35	1.0	5.3	31^{+12}_{-11}%
				1–6	42	2.3	6.0	33^{+13}_{-11}%
30–6000	598	74	20^{+2}_{-2}%	1–4	32	1.0	4.8	34^{+17}_{-13}%
				1–6	39	3.0	5.5	41^{+17}_{-14}%
158–6356	598	54	16^{+2}_{-2}%	1–4	32	0.8	4.4	24^{+13}_{-10}%
				1–6	39	1.2	5.1	25^{+13}_{-10}%

Note. Field and conditional DG occurrence rates under different planet definitions. The first DG mass limit is our nominal definition. The second and third match L. J. Rosenthal et al. (2022) and M. L. Bryan et al. (2019), respectively. We require that CS and DG planets have $a < 1$ au and $a = 1$–10 au, respectively. For the other two cases, we adopt the CS and/or DG separation limits given in L. J. Rosenthal et al. (2022; $a = 0.023$–1 au for CS and 0.23–10 au for DG) and M. L. Bryan et al. (2019; $a = 1$–20 au for DG). We calculate field occurrence rates using the CLS sample (L. J. Rosenthal et al. 2021), to which we apply a mass cut ($M_\star \geqslant 0.6\, M_\odot$) to exclude M dwarfs.

system. We did not find a significant difference between the period distributions of inner planets in trend systems and of single inner planets (i.e., those in systems with no resolved giant and no trend).

We note that using the first detected TOI in a system favors shorter separations in systems with multiple transiting planets. Thus, the pattern described above may be explained if outer giants are more likely to occur in systems with multiple inner planets (see Section 8.5).

8.4. Outer Companions May Have Preferentially Low Eccentricities

To evaluate the eccentricity distribution of our detected giants compared with the broader giant-planet population, we performed the following experiment. For each of the six resolved giants in our catalog, we drew one eccentricity value from a Gaussian distribution centered on the planet's median eccentricity and with standard deviation equal to the derived eccentricity uncertainty. We then recorded the mean of these six eccentricities. We repeated this process 1000 times, to account for the eccentricity uncertainty of each planet. We fit a Gaussian distribution to the average eccentricity values, finding that $\langle e_{sample} \rangle = 0.11 \pm 0.03$.

We used a similar process to quantify the eccentricities of DGs around field stars. We began with all planets in the NASA Exoplanet Archive (NEA)[30] that met our definition of a DG and had eccentricity uncertainty below 0.13, the maximum eccentricity uncertainty measured among the giants in our catalog. Note that we did not exclude giants with known inner

[30] https://exoplanetarchive.ipac.caltech.edu/

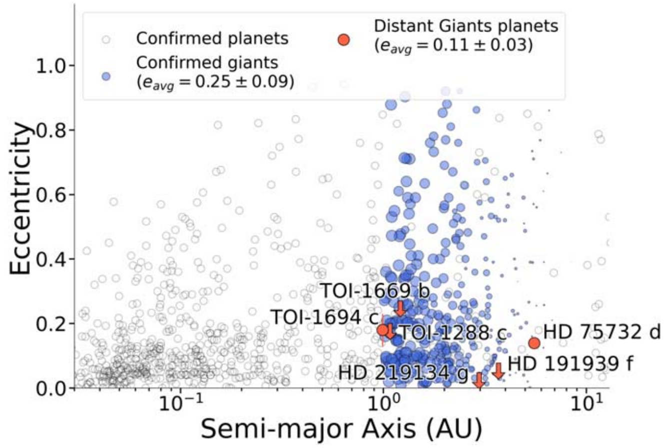

Figure 10. Distribution of eccentricity vs. orbital separation for confirmed exoplanets in the NEA with $\sigma_e \leqslant 0.13$. The confirmed planets are shown as unfilled circles and the confirmed DGs (1–10 au and 70–4000 $M_\oplus$) as blue circles. For confirmed giants, the marker size is proportional to our survey-averaged completeness at the planet's mass and separation. We show the giants in our survey in orange and indicate measurements with less than 3σ eccentricity precision with an arrow, placing the bottom of the arrow at the 1σ upper limit. The giant companions in our survey may have lower eccentricities than the average DG, but a larger sample is needed to draw a strong conclusion.

planets; because there are few systems hosting a confirmed giant and in which an inner planet can be ruled out at high significance, we chose to compute the field eccentricity distribution using all giants, irrespective of inner-planet presence. To match the six resolved giants in our catalog, we drew six random planets from this pool, with probability proportional to our measured completeness for each planet (see Figure 7). We then repeated the procedure we applied to our detected giants, obtaining a distribution of mean eccentricities for the six sampled giants. We again iterated this process by drawing 1000 such six-planet samples and calculating average eccentricity distributions for each of them. We found that the typical average eccentricity among a random sample of six planets from the NEA is $\langle e_{\rm field}\rangle = 0.25 \pm 0.09$.

We repeated this analysis with only the four resolved giants whose CS had $R_p < 4\,R_\oplus$ and found a similar result: $\langle e_{\rm sample}\rangle = 0.09 \pm 0.03$. Our findings show a discrepancy of $\sim 1.5\sigma$–2σ, indicating that the giants in our sample may have lower eccentricities than field giants. We show the distributions of the giant-planet eccentricities in Figure 10.

8.5. Systems with Multiple Transiting Planets May Be More Likely to Host an Outer Companion

Eight of the systems in our sample host more than one transiting planet. Four of these systems systems exhibit either a trend or a resolved orbit. We conducted a simple experiment to evaluate the statistical significance of the relationship between inner-planet multiplicity and outer-companion occurrence. We randomly drew 12 of the systems from our survey, corresponding to the number of companions detected in our catalog either as resolved orbits or as trends, and counted how many of them belonged to the subset of systems with multiple transiting planets. In 10% of our 10^4 experiments, four or more of the sampled systems had multiple inner planets. This finding corresponds to a p-value of 0.1, providing a tentative indication that the systems exhibiting resolved orbits or trends have multiple transiting planets more often than average.

Because the nature of the trend systems is uncertain, we repeated the above experiment using only the resolved systems, two of which host multiple inner planets. We drew six systems from our target list and calculated the fraction of times that two or more of them had multiple inner planets. In this case, there was no evidence of a correlation between inner-planet multiplicity and outer-giant presence ($p = 0.27$). We found similar results when considering only systems hosting inner planets with $R_p < 4\,R_\oplus$.

8.6. Outer-companion Occurrence Does Not Correlate with Stellar Parameters

We conducted KS tests for a variety of stellar parameters to see if they correlated with DG occurrence. We found no significant correlations between the resolved giants in our sample and $T_{\rm eff}$ ($p = 0.57$), $logR'_{\rm HK}$ ($p = 0.95$), or radius ($p = 0.94$). We found tentative evidence that stars hosting resolved giants have lower-than-average $v \sin i$ ($p = 0.06$) and higher-than-average stellar metallicity ($p = 0.09$), in agreement with the the established occurrence–metallicity relation (D. A. Fischer & J. Valenti 2005). We found similar results when restricting our analysis to the systems with transiting planets smaller than $4\,R_\oplus$.

9. Discussion

9.1. DG Occurrence

Our finding of a possible positive correlation between CS and DG planets is consistent with most previous studies of this relationship (W. Zhu & Y. Wu 2018; B19; R22). Each of these studies used different—though overlapping—target samples, compiled according to distinct criteria and analyzed by different methods, and although none was large enough to conclusively measure P(DG|CS), the overarching agreement between them points to a linked formation history between these classes.

We derived a lower enhancement factor of P(DG|CS) over P(DG) than prior works, which may be due to differences between our stellar sample and theirs. We constructed the DG sample using a uniform selection function, and we built up the RV baselines for most of our targets from scratch. Further, our requirement for transiting inner planets necessitated a more involved completeness correction to account for potential inclination biases. We expect that these choices resulted in higher accuracy in our inferred occurrence rates, but they also reduced statistical power, by restricting our sample size. Another possible explanation for our lower enhancement factor is our use of the CLS sample to calculate the DG field rate. W. Zhu (2022) found that the CLS sample has a hot-Jupiter abundance three times the commonly accepted value of $\sim 1\%$ (A. Cumming et al. 2008; M. Mayor et al. 2011; R. A. Wittenmyer et al. 2020). Given that hot Jupiters are frequently accompanied by a DG companion (J. K. Zink & A. W. Howard 2023), the overabundance of hot Jupiters in the CLS may also have led to an overabundance of DGs. Correcting for this effect could lower our calculated field occurrence, broadening the gap between P(DG) and P(DG|CS).

The recently completed Keck Giant Planet Search (KGPS; L. M. Weiss et al. 2024) is the largest survey (63 stars) yet used to address conditional giant-planet occurrence, and also targeted transiting planet hosts, with a uniform selection function and consistent observing strategy. Due to its similarity to the Distant Giants Survey, the KGPS will serve as a useful point of comparison for the results presented here.

We calculated our conditional and field occurrence rates using two different stellar samples, resulting in potential offsets stemming from different stellar parameter distributions (e.g., mass, metallicity, and temperature). The sample sizes of current long-baseline RV surveys ($\lesssim$1000 stars) limit the possibility of measuring both P(DG|CS) and P(DG) in a single sample. Large future surveys of statistically identical stellar samples will alleviate this problem, in addition to providing more accurate and precise occurrence measurements.

9.2. DGs and Metallicity

The occurrence–metallicity relation has been known for two decades: gas-giant planets are more prevalent around metal-rich stars (D. A. Fischer & J. Valenti 2005). This pattern implies that the high densities of solid material in the protoplanetary disks of metal-rich stars facilitate the formation of giant planets. Our study and others before it suggest that giants are also more prevalent in systems hosting an inner small planet.

A natural question is what the interplay between these two effects is. For example, do systems with a metal-rich host star and a close-in companion show the same relative enhancement over metal-rich field stars as non-metal-rich stars with close-in planets show over non-metal-rich field stars? Recently, M. L. Bryan & E. J. Lee (2024) reported an increased relative enhancement in metal-rich systems, suggesting that high-metallicity environments are especially well suited to producing DG–CS systems. In contrast, our findings suggest that metallicity does not strongly influence the relative enhancement; rather, our full sample exhibits a similar enhancement of DGs in the presence of CSs as the metal-rich sample.

9.3. DGs and Inner-planet Properties

A positive correlation between DGs and CSs could indicate that DGs help inner planets form, or that both planets develop independently in similar environments. Whether the DG–CS relation is causative may be encoded in the dynamical characteristics of the systems that host them.

In Section 8, we found preliminary evidence that, in systems with both an inner transiting planet and a DG, the inner planets have shorter-than-average periods, and the giants have lower-than-average eccentricities. If real, these patterns could shed light on the formation history of this class of systems. For example, these giants may have excited the eccentricities of their inner companions, initiating high-eccentricity migration to shorter periods through the eccentric von Zeipel–Lidov–Kozai mechanism (G. Li et al. 2014; S. Naoz 2016). On the other hand, this picture requires a high mutual inclination between the inner and outer planets, in tension with the possible overrepresentation of giants in multitransiting systems. Another explanation is that the giants underwent early type II disk migration (D. N. C. Lin & J. Papaloizou 1986), entraining gas and planetesimals in the inner disk and driving them to shorter separations (K. Batygin & G. Laughlin 2015).

We also found that outer giants may be more common in systems with multiple inner transiting planets. This is somewhat unexpected, given that a misaligned outer giant could dynamically perturb the multitransiting geometry (S. Naoz 2016). The fact that the system configurations endured suggests that their giants have low mutual inclinations. This feature, coupled with the observed tendency for giant companions to have lower eccentricities, points to a preference for CS–DG systems to either maintain or settle into dynamically cool final configurations, much like the solar system.

Obliquity offers another indication of dynamical evolution. Of the six systems hosting resolved outer giants, four have measurements of the sky-projected spin-orbit angle between the host star and the inner transiting planet: HD 191939 ($\lambda = 3.7 \pm 5°$—J. Lubin et al. 2024), HD 219134 ($\lambda = 0$–$20°$—C. P. Folsom et al. 2018), TOI-1694 ($\lambda = 9^{+22}_{-18}$ °—L. B. Handley et al. 2024), and HD 75732 ($\lambda = 10^{+17}_{-20}$ °—L. L. Zhao et al. 2023). The high degree of alignment in these systems comports with a picture involving low mutual inclinations and gentle planetary migration mechanisms. Obliquity measurements in the remaining two giant-hosting systems will test this pattern.

Many of the findings presented in this work are suggestive at the 2σ–3σ level but not statistically unassailable. To confirm or refute them, similar studies must be performed using larger stellar samples. For example, the number of TESS candidate hosts recently surpassed 7000, enabling the construction of a quadrupled (200-star) sample under our target selection criteria. Meanwhile, next-generation RV spectrographs—such as the Keck Planet Finder (S. R. Gibson et al. 2016), NEID (C. Schwab et al. 2016), and the Habitable Zone Planet Finder (S. Mahadevan et al. 2012) in the north, as well as ESPRESSO (F. Pepe et al. 2021) in the south—offer vastly improved throughput over their predecessors and more than enough precision to detect long-period giants. Their enhanced efficiency would permit a survey of an additional 150 systems using the same amount of telescope time needed to observe our original 47-star sample. Such a survey would open the door to conditional occurrence measurements at the 3σ–5σ level, providing dispositive evidence for or against a correlation.

Additionally, the fourth data release of the Gaia mission (Gaia Collaboration et al. 2016) is expected to yield tens of thousands of giant-companion detections (e.g., F. Feng 2024; A. L. Wallace et al. 2025). These detections will enable precise estimates of the field rate of super-Jupiter planets and, combined with small-planet detections from RV and/or transit missions, may help constrain their conditional occurrence as well.

9.4. Brown Dwarf Occurrence

The mass–separation prior we derived in Section 5.2 sheds light on the occurrence rate of brown dwarfs as a function of orbital separation. Our work takes advantage of the CLS's sensitivity to brown dwarfs at wide separations ($\lesssim$64 au), which extends into the discovery space of high-contrast imaging surveys at $\sim$5–1000 au (e.g., B. P. Bowler et al. 2020; B. P. Bowler & E. L. Nielsen 2018; G. Chauvin 2018). E. L. Nielsen et al. (2019) measured the prevalence of brown dwarfs from 10 to 100 au, finding that $0.8^{+0.8}_{-0.5}$% of stars host such a companion. They also found that brown dwarfs and giant planets (5–13 M_J) exhibit different semimajor-axis distributions, with planets peaking in occurrence between 1 and 10 au and brown dwarfs favoring wider separations.

We integrated our mass–separation prior between 13–80 M_J and 10–30 au, finding that brown dwarfs occur at a rate of 1.6 per 100 stars in this interval. Using the simplifying assumption that the occurrence rate is log-uniform out to 100 au, we estimate that 3.2% of stars host a brown dwarf between 10 and 100 au, significantly greater than the finding of E. L. Nielsen et al. (2019) over the same interval. On the other hand, we observed a distinction between giant-planet and brown dwarf occurrence, in agreement with E. L. Nielsen et al. (2019). We found that giant planets, which we define as having $M = 3$–$13\ M_{\rm J}$, peak in occurrence in the interval 1–4 au and decline at greater separations. By contrast, brown dwarf occurrence may increase at greater separations, reaching its maximum in the interval 16–64 au. Like the distinct eccentricity distributions between brown dwarfs and giant planets fit by B. P. Bowler et al. (2020), our finding of disparate separation distributions supports the idea that these objects follow different formation pathways. We note that our brown dwarf occurrence-rate value of 3.2% is based on a significant extrapolation of the RV-derived occurrence rates in order to produce a consistent comparison with E. L. Nielsen et al. (2019). More work is needed to perform a comparison without extrapolation.

It is important to note that a number of effects may have influenced our calculated occurrence rates. First, stellar companions on inclined orbits may masquerade as lower-mass objects in RV surveys. We simulated this effect by applying random orbital orientations to a set of stars following the distribution of D. Raghavan et al. (2010). We found that, on average, one of the nine brown dwarfs we used in our calculation was likely to be a star, insufficient to explain the disagreement with E. L. Nielsen et al. (2019). Nevertheless, the small number of brown dwarfs means that significant contamination remains a possibility. Second, despite its multidecade baseline, the CLS has limited sensitivity to companions at tens of astronomical units. Many of the detections are partial orbits with large mass and separation uncertainties, and they may therefore not fall within the bin in which we counted them. For example, the mass of HD 28185 c was recently revised from $40^{+43}_{-28}\,M_{\rm J}$ to $6 \pm 0.6\,M_{\rm J}$ through the incorporation of HGCA astrometry (A. Venner et al. 2024). We reserve a more detailed analysis and a firmer conclusion for future work.

10. Conclusion

We have presented the results of a 3 yr RV survey to search for outer giant planets around 47 Sun-like stars with known inner planets. Our final catalog includes six RV trends and six well-characterized giants. We have incorporated all of these detections into a Poisson likelihood model to calculate the conditional occurrence of DGs in the presence of CSs, P(DG|CS). We corrected for missed planets by characterizing our detection sensitivity in each system. We found that $31^{+12}_{-11}\%$ of stars that host a CS ($a < 1$ au, $R_p \leqslant 4R_\oplus$) also host a DG ($a = 1$–10 au, $M_p \sin i = 70 - 4000 M_\oplus$). Meanwhile, using the larger CLS sample of L. J. Rosenthal et al. (2021), we determined that between $16^{+2}_{-2}\%$ and $18^{+2}_{-2}\%$ of stars host a DG planet irrespective of the presence of CSs. Our findings give tentative evidence for a 1.5–2 times enhancement of giants in CS-hosting systems, suggesting that outer giants and inner small planets may be positively correlated, with giants even promoting the formation of inner planets.

Sample size and homogeneity are vital components of a precise and accurate measurement of conditional giant occurrence. Studies of this topic to date, including this one, have had to prioritize one of these components at the expense of the other. However, advancements over the last few years have made possible a dramatic increase in sample size without compromising sample purity. Making use of this progress will bring the nuances of planetary formation into sharper focus.

Acknowledgments

We thank the reviewer for providing helpful comments that improved this study. J.V.Z. acknowledges support from NASA FINESST Fellowship 80NSSC22K1606. J.V.Z. and E.A.P. acknowledge support from NASA XRP award 80NSSC21K0598. J.M.A.M. is supported by the National Science Foundation (NSF) Graduate Research Fellowship Program (GRFP) under Grant No. DGE-1842400. J.M.A.M. and N.M.B. acknowledge support from NASA'S Interdisciplinary Consortia for Astrobiology Research (NNH19ZDA001N-ICAR) under award number 19-ICAR19_2-0041. E.V.T. acknowledges support from a David & Lucile Packard Foundation grant. T.F. acknowledges support from an appointment through the NASA Postdoctoral Program at the NASA Astrobiology Center, administered by Oak Ridge Associated Universities under contract with NASA. M.L.H. would like to acknowledge NASA support via the FINESST Planetary Science Division, NASA award number 80NSSC21K1536.

This work was supported by NASA Keck PI Data Awards and NASA Key Project Mission Support proposals administered by the NASA Exoplanet Science Institute. Data presented herein were obtained at the W. M. Keck Observatory, from telescope time allocated to the National Aeronautics and Space Administration through the agency's scientific partnership with the California Institute of Technology and the University of California. The Observatory was made possible by the generous financial support of the W. M. Keck Foundation.

The authors wish to recognize and acknowledge the very significant cultural role and reverence that the summit of Maunakea has always had within the indigenous Hawaiian community. We are most fortunate to have the opportunity to conduct observations from this mountain.

Appendix A
Companions Detected as Trends

A.1. TOI-1174

TOI-1174 is a K2 dwarf at a distance of 95 pc, hosting a transiting $2.3\,R_\oplus$ sub-Neptune with a 9.0 days period. We measured an RV trend and curvature of -27.48 ± 5.97 m s^{-1} yr^{-1} and 14.48 ± 2.89 m s^{-1} yr^{-2} in this system, indicating the presence of an outer companion (Figure A1). Although we were unable to precisely constrain a and M_p in this system, due to the lack of astrometry data, 832 nm speckle imaging observations from the 'Alopeke imager coupled to the 8 m Gemini North telescope (N. J. Scott et al. 2021), and reduced according to S. B. Howell et al. (2011), ruled out luminous companions beyond ∼40 au and more massive than $\sim 200\,M_{\rm J}$. We depict the direct imaging constraints by converting the measured contrast curves to mass–separation space, assuming circular face-on orbits for simplicity, as explained in J. Van Zandt & E. Petigura (2024a). We found that the source of the measured RV variability is most likely planetary: P(planet) = 53%.

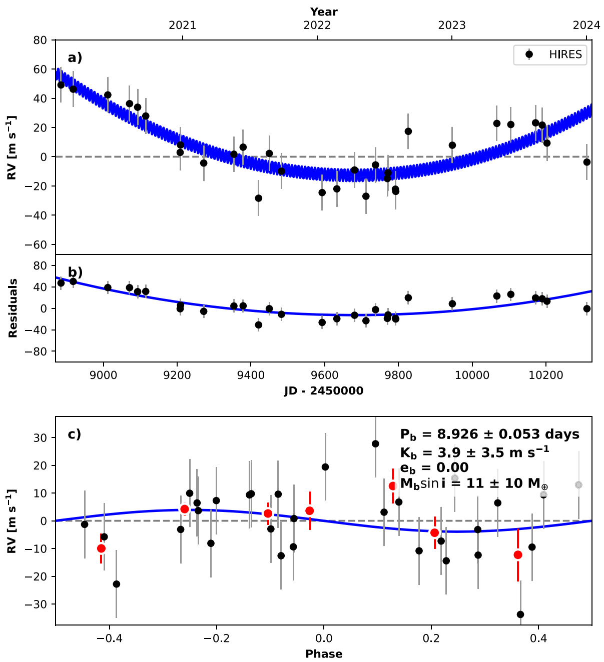

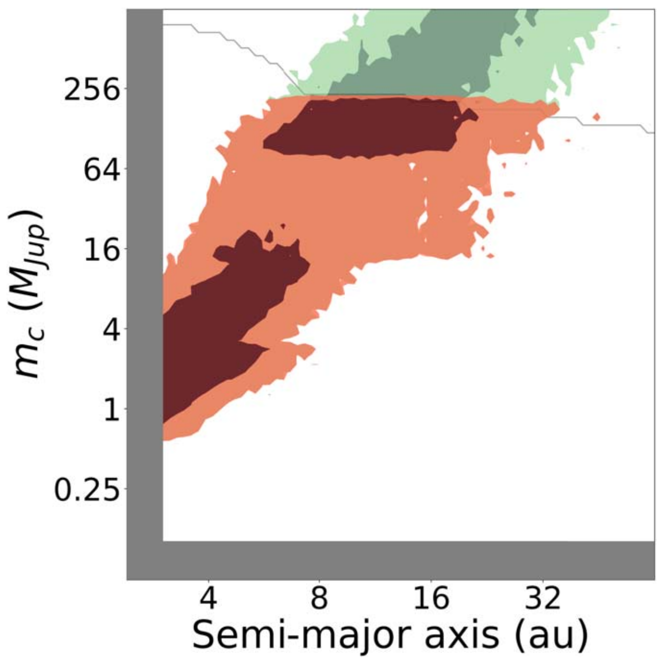

Figure A1. Left: our orbital fit to the TOI-1174 system using `radvel`. (a) The full RV time series and errors with black circles, with our preferred model as a blue line. (b) The residuals to the planetary model, isolating the fitted trend/curvature. (c) The RV time series phase-folded to the period of the inner planet in this system. The red points give binned RV values. We did not recover the inner-transiting-planet signal in the RVs. Right: our `ethraid` posterior surface derived using the measured trend. The green regions show models consistent with the RV trend, and the red regions show models consistent with both the RVs and the direct imaging for this system, revealing no luminous companions. The dark (light) regions indicate 68% (95%) confidence intervals. The gray line approximates the contrast limits imposed by imaging for a circular, face-on companion. The gray panels at low mass and short separations show companion parameters incompatible with the observed trend due to our observing baseline.

A.2. HD 191939

HD 191939 is a G0 dwarf 54 pc away hosting three transiting sub-Neptunes with periods of 8.9, 28.6, and 38.4 days. Multiple studies have probed this system with RVs (M. Badenas-Agusti et al. 2020; J. Lubin et al. 2022, 2024), resulting in mass measurements of the transiting planets, a determination that the system is aligned, and the discovery of a 100 days super-Saturn (e) and an 8 yr super-Jupiter (f). We truncated this system's time series to 4 yr, causing HD 191939 f to present as a trend. We combined this trend with an HGCA astrometric acceleration of 0.13 ± 0.03 mas yr^{-1}, which resulted in a 98% probability that the trend's origin is planetary. We included adaptive optics imaging from Gemini/NIRI in our analysis, though it does not rule out any companion models. Figure A2 shows our orbital fit and trend analysis for this system. Our automated search algorithm recovered planet e, as well as a spurious 900 days planet. This planet demonstrates a shortcoming of our automated algorithm, which is not designed to be sensitive to multiple signals. Nevertheless, with an RV semi-amplitude of 3.2 m s^{-1}, it did not detract significantly from the signal of planet f, which has $K = 47$ m s^{-1}.

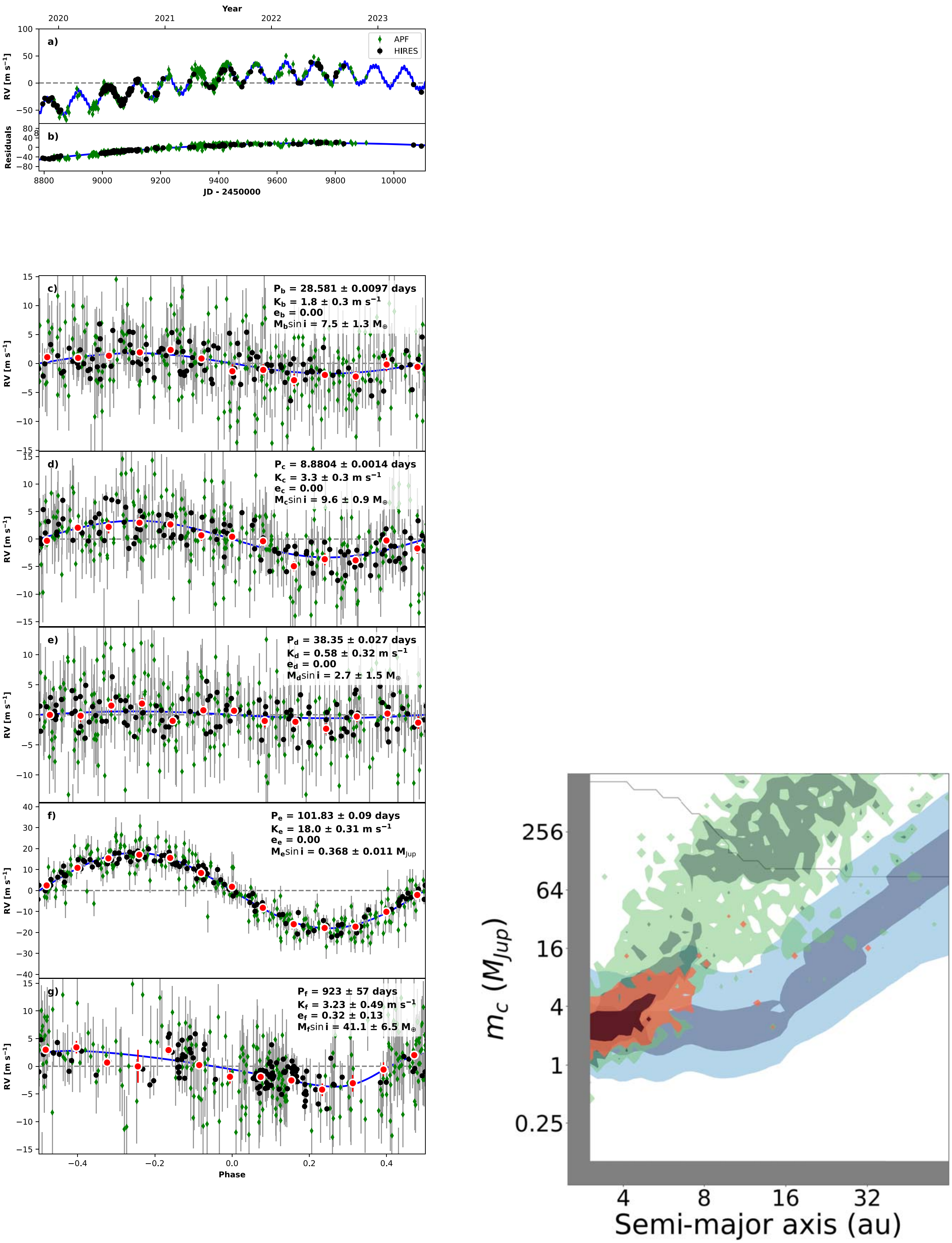

Figure A2. The same as Figure A1 but for HD 191939. We included the three transiting planets in our model, and our blind search algorithm detected the known 100 days super-Saturn as well as a spurious long-period planet. The blue posterior surface shows constraints imposed by the astrometric acceleration measured in this system. The trend and curvature in our truncated RV time series along with the astrometric acceleration yield a high planetary odds ratio.

A.3. TOI-1438

TOI-1438 is a K1 dwarf at 111 pc hosting two transiting sub-Neptunes, the inner of which has a radius of $3.0\,R_\oplus$ and a period of 5.1 days (C. Persson et al. 2025, in preparation). TOI-1438 showed the largest RV trend in our sample: $\dot{\gamma} = 41.41 \pm 3.41\ \mathrm{m\,s^{-1}\,yr^{-1}}$, $\ddot{\gamma} = -13.65 \pm 1.40\ \mathrm{m\,s^{-1}\,yr^{-2}}$ (Figure A3). Our trend analysis, along with 832 nm speckle imaging from 'Alopeke, indicated that these signals may originate from a planet (79%), brown dwarf (8%), or stellar companion (12%).

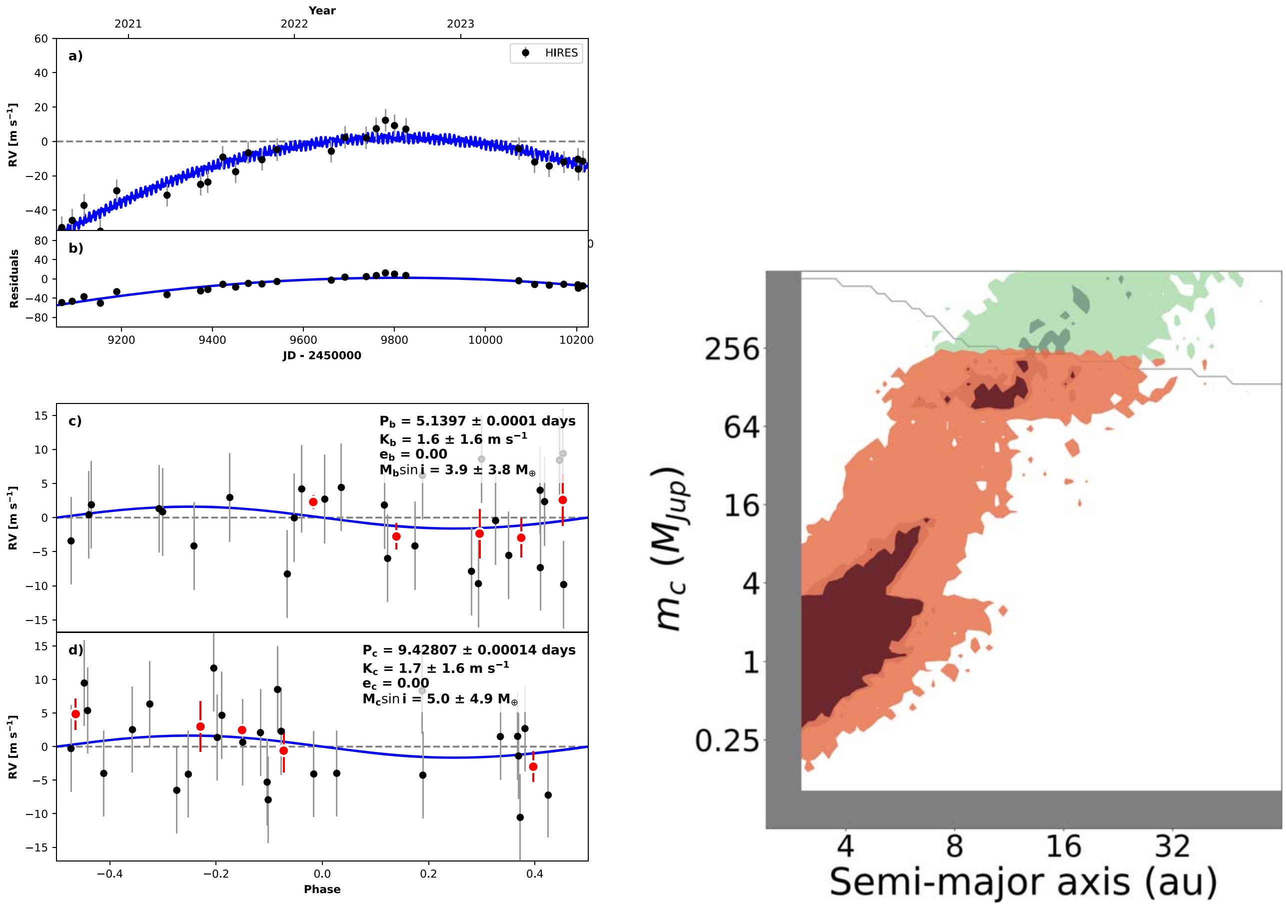

Figure A3. The same as Figure A1 but for TOI-1438. We were unable to detect the transiting planets in this system, but we measured a strong trend and curvature, consistent with planetary, brown dwarf, or stellar companion models.

A.4. HD 219134

HD 219134 is a nearby (6.5 pc) K3 dwarf hosting two transiting super-Earths with periods of 3.1 and 6.8 days. This system has been observed for multiple decades, providing detections of four additional planets, including a 6 yr super-Saturn, meeting our DG definition (S. S. Vogt et al. 2015). As with HD 191939, we truncated this system's baseline to 4 yr and performed our blind search. We tested the dependence of our results on our choice of truncation window and found that it had a negligible effect. Our automated algorithm detected the 47 days Neptune analog (e) but missed a known super-Earth with a 23 days period (d) and a 94 days super-Earth (f). It also found a strong trend due to HD 219134 g, which we analyzed together with an HGCA acceleration to find a high planetary odds ratio of P(planet) $\sim$ 100%. Figure A4 shows the results of our full and partial orbit fits.

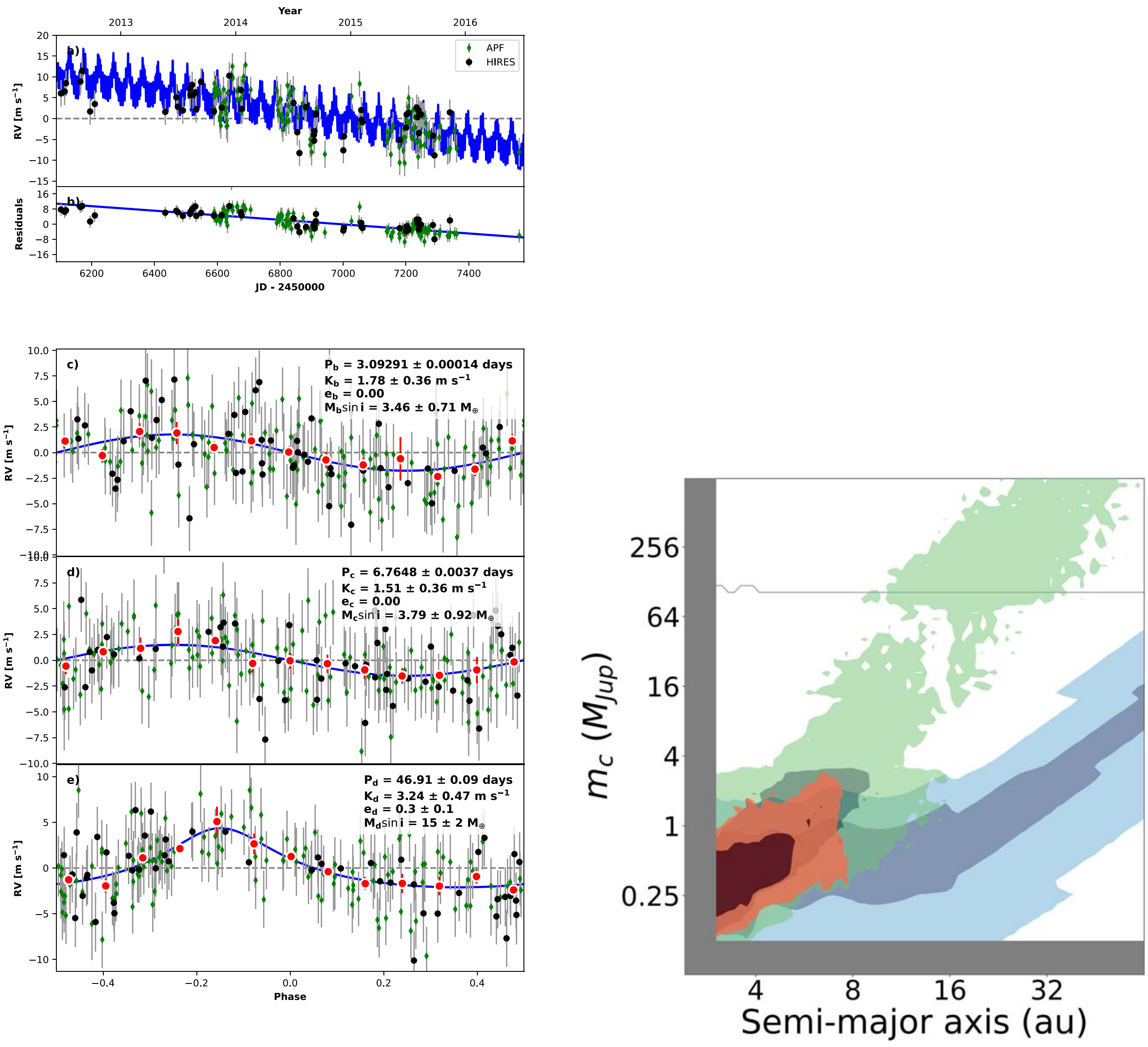

Figure A4. The same as Figure A1 but for HD 219134. We chose RV measurements from an arbitrary 4 yr span of this system's full data set. We recovered one of the nontransiting planets using a blind search but missed two others. We analyzed the measured trend and HGCA astrometry to calculate a probability near 1 of this signal originating from a planet. We also tested other 4 yr spans and verified that our choice did not strongly influence our final odds ratio.

A.5. HD 12572

HD 12572 is a G9 dwarf at a distance of 73 pc hosting two transiting sub-Neptunes. The inner planet, HD 12572 b, has a radius of 3.9 $R_{\oplus}$ and a 20.8 days period (H. P. Osborn et al. 2023). This star's high brightness ($V = 9.2$) allowed us to obtain contemporaneous APF RVs alongside our HIRES observations. We measured an RV trend and curvature of -22.09 ± 2.11 m s^{-1} yr^{-1} and -0.05 ± 0.73 m s^{-1} yr^{-2} in this system, as well as a marginally significant astrometric acceleration of $\Delta\mu = 0.07 \pm 0.05$ mas yr^{-1}(Figure A5). Coupled with Br γ (2.16 μm) direct imaging from NIRC2, we calculated a 61% probability that the outer companion in this system is a planet. Our results are in tension with H. P. Osborn et al. (2023), who concluded that the outer companion is a brown dwarf between 15 and 50 au. This disagreement may be due in part to our informative mass prior, which disfavors brown dwarf companions.

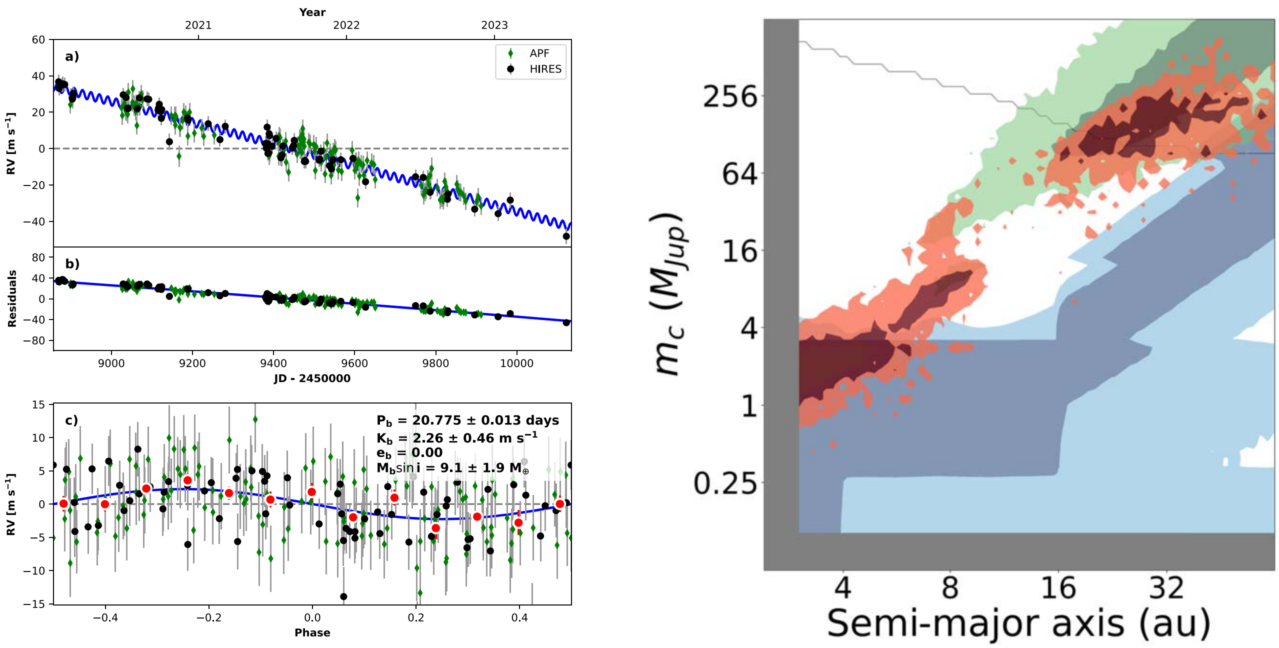

Figure A5. The same as Figure A1 but for HD 12572. We measured the mass of the 20 days sub-Neptune in this system and also found a strong linear trend with no significant curvature. We also measured a marginal astrometric acceleration, which imposed added constraints (blue contours). Note that the gray line denotes orbital models that are ruled out by direct imaging under the assumption of a circular, face-on orbit. Companions with nonzero inclinations and eccentricities may lie beyond the line without being ruled out.

A.6. HD 156141

HD 156141 is a solar analog (G2) at a distance of 73 pc hosting a transiting $2.2\,R_\oplus$ sub-Neptune with a 21.3 days period. We measured an RV trend and curvature of $30.20 \pm 1.87\,\mathrm{m\,s^{-1}\,yr^{-1}}$ and $-7.22 \pm 0.72\,\mathrm{m\,s^{-1}\,yr^{-2}}$, and ruled out high-mass stellar models using NIRC2 Br γ imaging (Figure A6). We found that the outer companion in this system has a 78% probability of being a planet.

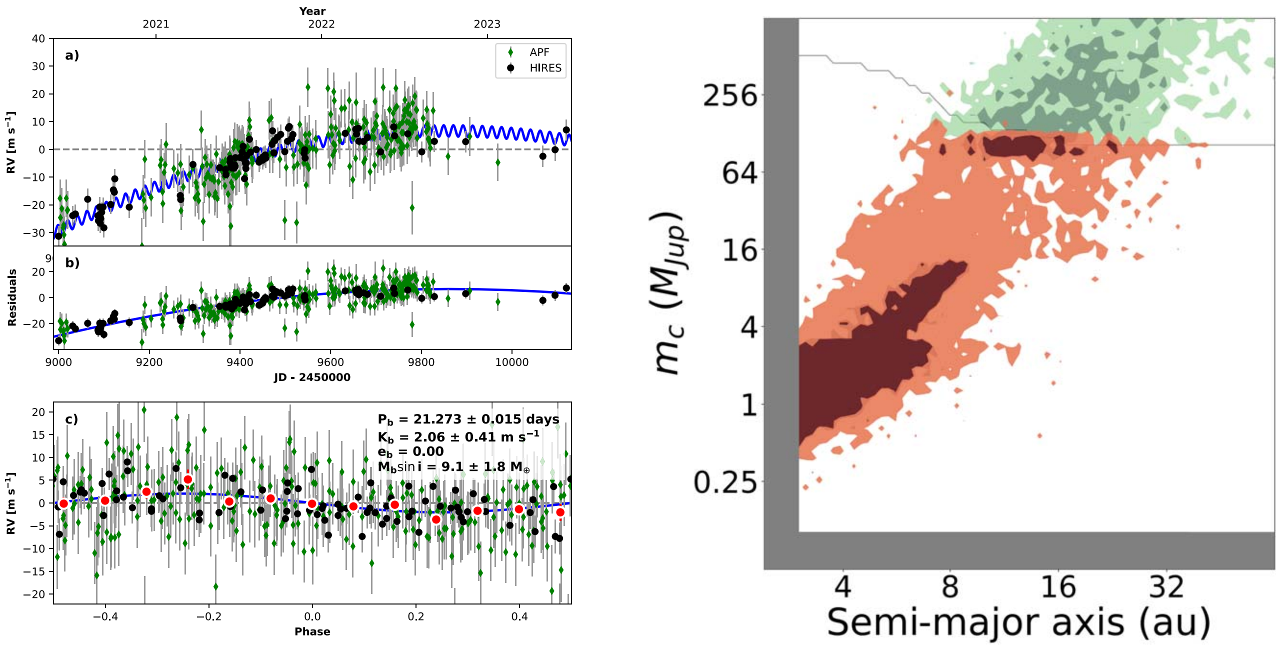

Figure A6. The same as Figure A1 but for HD 156141. We obtained a marginally significant measurement of the inner transiting planet's mass and high-significance trend and curvature measurements. The long-term signals in this system are consistent with planets and brown dwarfs, whereas stellar models are nearly ruled out with the aid of direct imaging.

A.7. HD 75732

HD 75732 is a nearby (12.5 pc) K0 dwarf hosting a transiting ultrashort-period (0.74 days) super-Earth. Like HD 219134, this system is well characterized from decades of RV observation (e.g., D. A. Fischer et al. 2008). We chose an arbitrary 4 yr window over which to fit these RVs and verified that our choice did not significantly impact our characterization of the outer planet. We detected the hot Jupiter HD 75732 b but did not detect the four other nontransiting planets. The outermost of these, a super-Jupiter with a period of nearly 14 yr, manifested as a trend in our truncated RV time series. We combined this trend with a marginal detection of HGCA acceleration to constrain the companion's mass and separation. Our analysis indicates that the trend is almost certainly planetary, with P(planet) ∼91%. We show our orbital fit and partial orbit analysis in Figure A7.

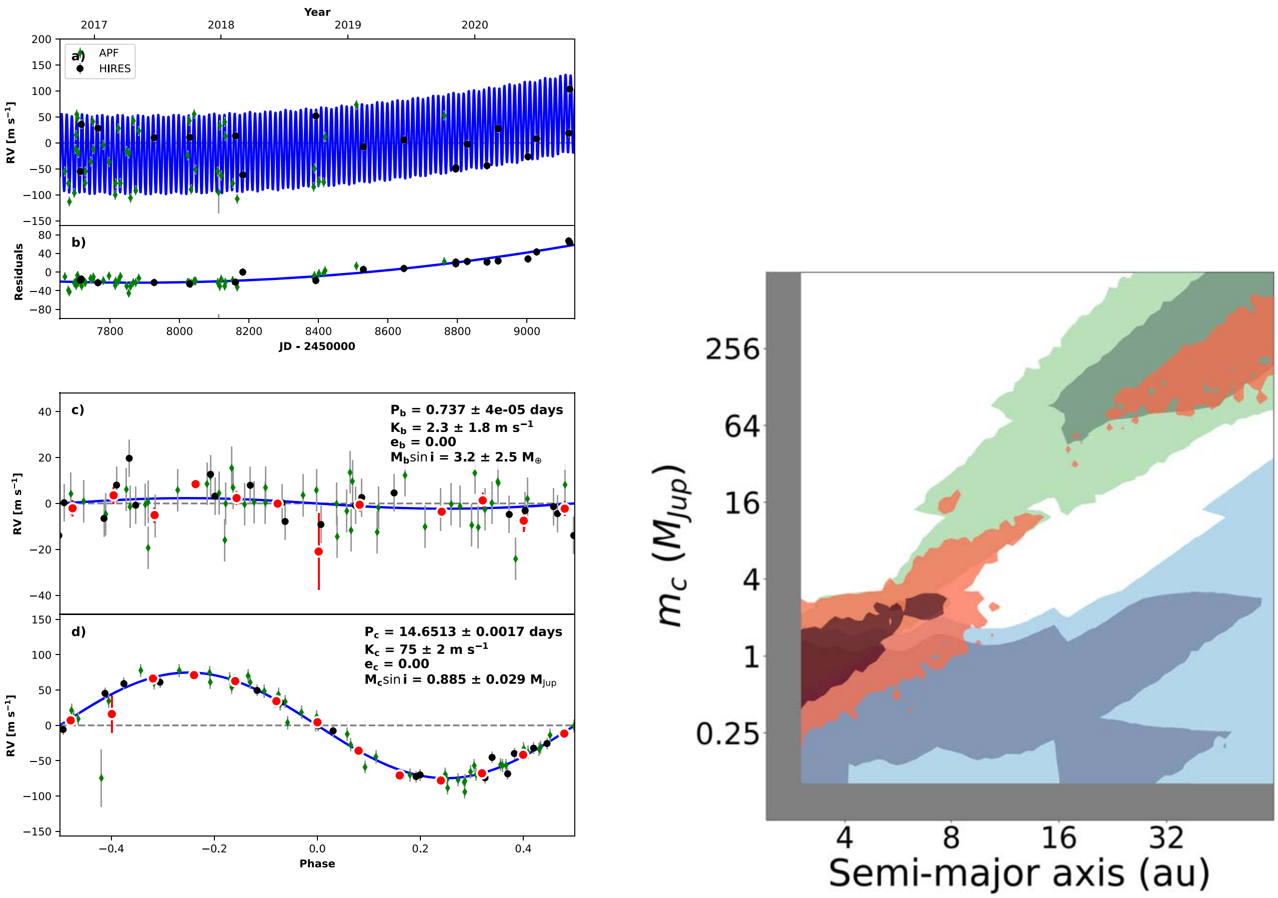

Figure A7. The same as Figure A1 but for HD 75732. We detected only one of the four nontransiting planets in this system using our blind search algorithm. The residual trend, together with a low-significance astrometric acceleration, constrain the mass–separation posterior primarily to the planetary regime.

A.8. HD 93963

HD 93963 A is a G2 dwarf at a distance of 83 pc hosting a transiting $3.2\,R_\oplus$ sub-Neptune with a 3.6 days period (L. M. Serrano et al. 2022). Our measured RV trend and curvature of $-10.51 \pm 2.66\,\mathrm{m\,s^{-1}\,yr^{-1}}$ and $-7.50 \pm 3.55\,\mathrm{m\,s^{-1}\,yr^{-2}}$, together with 832 nm speckle imaging from 'Alopeke, indicate an 81% probability of a planetary outer companion (Figure A8). L. M. Serrano et al. (2022) estimated that the stellar companion to this star, HD 93963 B, has a separation of ⩾484 au and a spectral type of M5 V (≈170 M_J; M. J. Pecaut & E. E. Mamajek 2013). We show in Figure A9 that a companion of that mass and separation is incompatible with the measured RV signature.

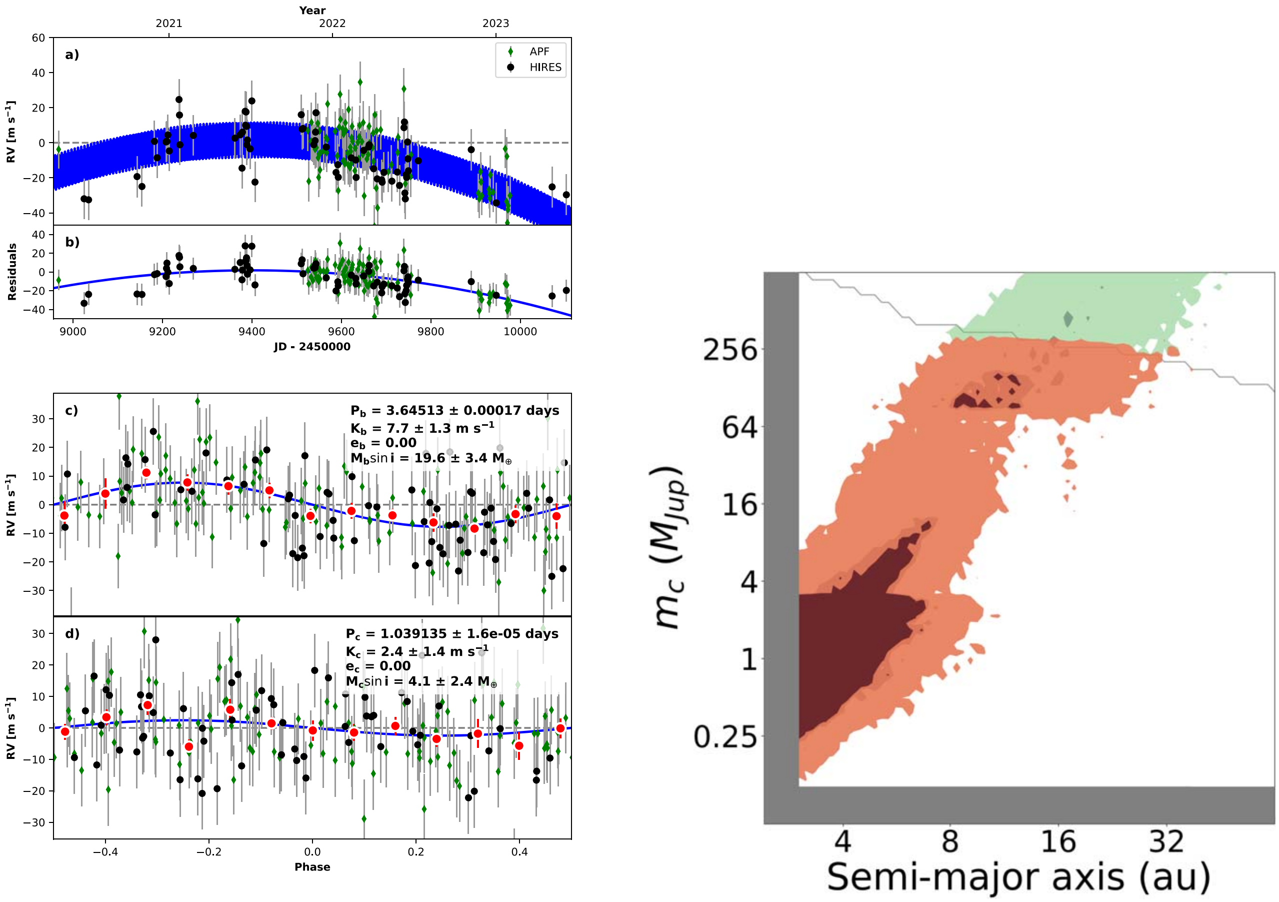

Figure A8. The same as Figure A1 but for HD 93963. We did not recover either of this system's two transiting planets at high significance. We measured a significant trend and marginal curvature in this system. Our analysis showed that the source of this RV variability is most likely a planet.

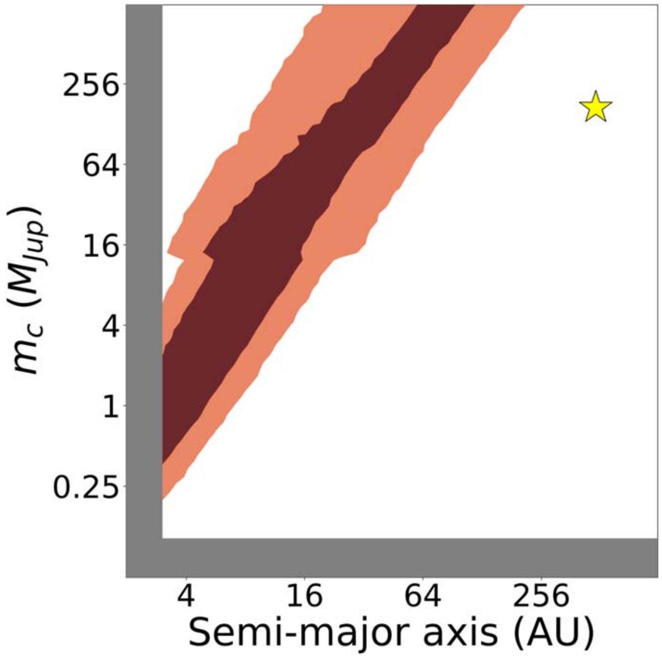

Figure A9. Our second analysis of the trend in the HD 93963 system. We expanded the semimajor-axis range over which we tested companion models and therefore did not use the informative mass–separation prior described in Section 5.2, which is defined for separations ⩽64 au. We indicate the position of the stellar companion, HD 93963 B, with a yellow star. Our analysis suggests that an M5 dwarf at a separation of 484 au is too small/too distant to have caused the observed trend.

A.9. TIC 142381532

TIC 142381532 is a K0 dwarf 72 pc away hosting a transiting 8.1 $R_{\oplus}$ sub-Saturn with a 38.8 days period (A. S. Polanski et al. 2024). We measured an RV trend and curvature of $-13.99 \pm 4.60\,\mathrm{m\,s^{-1}\,yr^{-1}}$ and $1.79 \pm 1.27\,\mathrm{m\,s^{-1}\,yr^{-2}}$, and used 832 nm speckle imaging from 'Alopeke to rule out high-mass stellar companions (Figure A10). We calculated a 32% probability that the measured signals originate from a planet. Despite passing our original radius filter of $R_p < 10R_{\oplus}$, the transiting planet in this system does not fit most definitions of a "small" planet. We include it for completeness but exclude it from our conditional occurrence calculations.

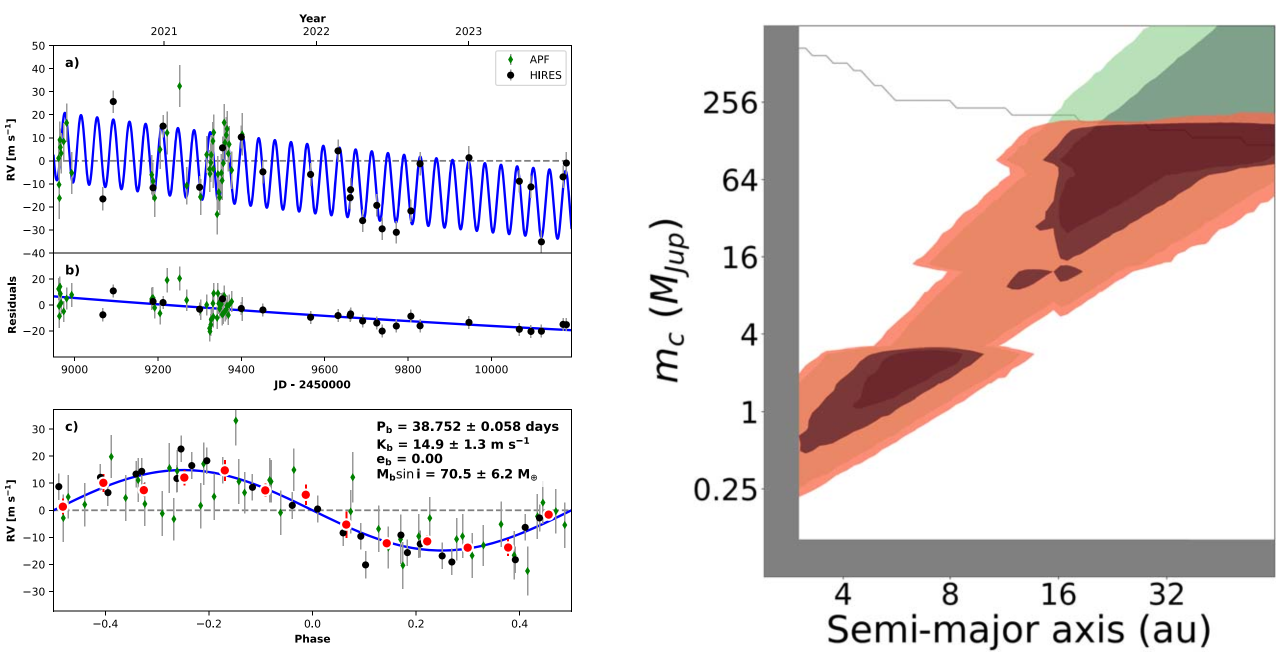

Figure A10. The same as Figure A1 but for TIC 142381532. The inner transiting planet in this system in a sub-Saturn, which we characterized at high significance. Although this planet passed $R_p < 10\,R_{\oplus}$, it is likely a gas giant, so we exclude this system from our occurrence calculations. Our trend measurement is marginal and evinces planetary and brown dwarf models with roughly equal probability.

Appendix B
Transiting Planet Properties

We provide stellar and transiting planet parameters for the Distant Giants sample in Table B1.

Table B1
DG Sample

TOI	TKS Name	R.A. (deg)	Decl. (deg)	V	T_{eff}	[Fe/H]	R_p ($R_\oplus$)	P (days)	DG?	Trend?
465	WASP156	32.8	2.4	11.6	5032	0.29	5.6	3.8	X	X
509	63935	117.9	9.4	8.6	5534	0.09	3.1	18.1	X	X
1173	T001173	197.7	70.8	11.0	5352	0.18	9.2	7.1	X	X
1174	T001174	209.2	68.6	11.0	5124	0.00	2.3	9.0	X	✓
1180	T001180	214.6	82.2	11.0	4790	−0.01	2.8	9.7	X	X
1194	T001194	167.8	70.0	11.3	5428	0.33	8.9	2.3	X	X
1244	T001244	256.3	69.5	11.9	4675	−0.04	2.4	6.4	X	X
1246	T001246	251.1	70.4	11.6	5158	0.17	3.3	18.7	X	X
1247	135694	227.9	71.8	9.1	5648	−0.13	2.8	15.9	X	X
1248	T001248	259.0	63.1	11.8	5272	0.22	6.6	4.4	X	X
1249	T001249	200.6	66.3	11.1	5514	0.29	3.2	13.1	X	X
1255	HIP97166	296.2	74.1	9.9	5214	0.28	2.7	10.3	X	X
1269	T001269	249.7	64.6	11.6	5466	−0.06	2.4	4.3	X	X
1272	T001272	199.2	49.9	11.8	5091	0.21	4.3	3.3	X	X
1279	T001279	185.1	56.2	10.7	5414	−0.10	2.6	9.6	X	X
1288	T001288	313.2	65.6	10.4	5357	0.26	4.7	2.7	✓	X
1339	191939	302.0	66.9	9.0	5355	−0.15	3.2	8.9	✓	X
1410	T001410	334.9	42.6	11.1	4666	0.16	2.9	1.2	X	X
1411	GJ9522A	232.9	47.1	10.5	4478	−0.10	1.4	1.5	X	X
1422	T001422	354.2	39.6	10.6	5852	−0.03	3.1	13.0	X	X
1437	154840	256.1	56.8	9.2	6049	−0.19	2.4	18.8	X	X
1438	T001438	280.9	74.9	11.0	5234	0.08	2.8	5.1	X	✓
1443	T001443	297.4	76.1	10.7	5160	−0.30	2.1	23.5	X	X
1444	T001444	305.5	70.9	10.9	5466	0.14	1.3	0.5	X	X
1451	T001451	186.5	61.3	9.6	5735	−0.01	2.5	16.5	X	X
1469	219134	348.3	57.2	5.6	4839	0.11	1.2	3.1	✓	X
1471	12572	30.9	21.3	9.2	5599	−0.03	4.3	20.8	X	✓
1472	T001472	14.1	48.6	11.3	5186	0.28	4.3	6.4	X	X
1611	207897	325.2	84.3	8.4	5091	−0.04	2.7	16.2	X	X
1669	T001669	46.0	83.6	10.2	5551	0.26	2.2	2.7	✓	X
1691	T001691	272.4	86.9	10.1	5689	0.03	3.8	16.7	X	X
1694	T001694	97.7	66.4	11.4	5069	0.12	5.5	3.8	✓	X
1710	T001710	94.3	76.2	9.5	5734	0.15	5.4	24.3	X	X
1716	237566	105.1	56.8	9.4	5861	0.06	2.7	8.1	X	X
1723	T001723	116.8	68.5	9.7	5800	0.16	3.2	13.7	X	X
1742	156141	257.3	71.9	8.9	5733	0.18	2.2	21.3	X	✓
1751	146757	243.5	63.5	9.3	5961	−0.38	2.8	37.5	X	X
1753	T001753	252.5	61.2	11.8	5620	0.03	3.0	5.4	X	X
1758	T001758	354.7	75.7	10.8	5142	−0.03	3.8	20.7	X	X
1759	T001759	326.9	62.8	11.9	4420	−0.20	3.2	37.7	X	X
1773	75732	133.1	28.3	6.0	5363	0.42	1.8	0.7	✓	X
1775	T001775	150.1	39.5	11.6	5349	0.19	8.1	10.2	X	X
1794	T001794	203.4	49.1	10.3	5663	0.02	3.0	8.8	X	X
1797	93963	162.8	25.6	9.2	5948	0.10	3.2	3.6	X	✓
1823	TIC142381532	196.2	63.8	10.7	4917	0.28	8.1	38.8	X	✓
1824	T001824	197.7	61.7	9.7	5216	0.12	2.4	22.8	X	X
2088	T002088	261.4	75.9	11.6	4902	0.31	3.5	124.7	X	X

Note. The properties of the 47 stars in the DG sample, plus the periods and radii of their inner companions. For multitransiting systems, we checked the planets in the order that TESS detected them and show the properties of the first one that passed our filters. We truncated period precisions for readability. The median uncertainties are as follows: [Fe/H]–0.06-0.09 dex; R_p—9.6%; and P—60 ppm. We calculated metallicity values using the `SpecMatch-Synthetic` code (E. A. Petigura 2015) for host stars with $T_{\mathrm{eff}} > 4800$ K ($\sigma_{[\mathrm{Fe/H}]} = 0.06$ dex). We used `SpecMatch-Empirical` (S. W. Yee et al. 2017) for host stars above this limit ($\sigma_{[\mathrm{Fe/H}]} = 0.09$ dex). We retrieved all other values from A. Chontos et al. (2022). We also indicate in the two rightmost columns which systems exhibit either a fully resolved giant-planet signal or a long-term RV trend.

ORCID iDs

Judah Van Zandt https://orcid.org/0000-0002-4290-6826
Erik A. Petigura https://orcid.org/0000-0003-0967-2893
Jack Lubin https://orcid.org/0000-0001-8342-7736
Lauren M. Weiss https://orcid.org/0000-0002-3725-3058
Emma V. Turtelboom https://orcid.org/0000-0002-1845-2617
Tara Fetherolf https://orcid.org/0000-0002-3551-279X
Joseph M. Akana Murphy https://orcid.org/0000-0001-8898-8284
Gregory J. Gilbert https://orcid.org/0000-0003-0742-1660
Teo Močnik https://orcid.org/0000-0003-4603-556X
Natalie M. Batalha https://orcid.org/0000-0002-7030-9519
Courtney Dressing https://orcid.org/0000-0001-8189-0233
Benjamin Fulton https://orcid.org/0000-0003-3504-5316
Andrew W. Howard https://orcid.org/0000-0001-8638-0320
Daniel Huber https://orcid.org/0000-0001-8832-4488
Howard Isaacson https://orcid.org/0000-0002-0531-1073
Stephen R. Kane https://orcid.org/0000-0002-7084-0529
Paul Robertson https://orcid.org/0000-0003-0149-9678
Arpita Roy https://orcid.org/0000-0001-8127-5775
Isabel Angelo https://orcid.org/0000-0002-9751-2664
Aida Behmard https://orcid.org/0000-0003-0012-9093
Corey Beard https://orcid.org/0000-0001-7708-2364
Ashley Chontos https://orcid.org/0000-0003-1125-2564
Fei Dai https://orcid.org/0000-0002-8958-0683
Steven Giacalone https://orcid.org/0000-0002-8965-3969
Michelle L. Hill https://orcid.org/0000-0002-0139-4756
Rae Holcomb https://orcid.org/0000-0002-5034-9476
Steve B. Howell https://orcid.org/0000-0002-2532-2853
Andrew W. Mayo https://orcid.org/0000-0002-7216-2135
Daria Pidhorodetska https://orcid.org/0000-0001-9771-7953
Alex S. Polanski https://orcid.org/0000-0001-7047-8681
James Rogers https://orcid.org/0000-0001-7615-6798
Lee J. Rosenthal https://orcid.org/0000-0001-8391-5182
Ryan A. Rubenzahl https://orcid.org/0000-0003-3856-3143
Nicholas Scarsdale https://orcid.org/0000-0003-3623-7280
Dakotah Tyler https://orcid.org/0000-0003-0298-4667
Samuel W. Yee https://orcid.org/0000-0001-7961-3907
Jon Zink https://orcid.org/0000-0003-1848-2063

References

Badenas-Agusti, M., Günther, M. N., Daylan, T., et al. 2020, AJ, 160, 113
Batygin, K., & Laughlin, G. 2015, PNAS, 112, 4214
Bonomo, A. S., Dumusque, X., Massa, A., et al. 2023, A&A, 677, A33
Bowler, B. P., Blunt, S. C., & Nielsen, E. L. 2020, AJ, 159, 63
Bowler, B. P., & Nielsen, E. L. 2018, in Handbook of Exoplanets, ed. H. J. Deeg & J. A. Belmonte (Cham: Springer), 155
Brandt, T. D. 2021, ApJS, 254, 42
Bryan, M. L., Knutson, H. A., Lee, E. J., et al. 2019, AJ, 157, 52
Bryan, M. L., & Lee, E. J. 2024, ApJL, 968, L25
Chauvin, G. 2018, Proc. SPIE, 10703, 1070305
Chen, J., & Kipping, D. 2017, ApJ, 834, 17
Chiang, E., & Laughlin, G. 2013, MNRAS, 431, 3444
Chontos, A., Murphy, J. M. A., MacDougall, M. G., et al. 2022, AJ, 163, 297
Cumming, A., Butler, R. P., Marcy, G. W., et al. 2008, PASP, 120, 531
Dawson, R. I., & Fabrycky, D. C. 2010, ApJ, 722, 937
Feng, F. 2024, arXiv:2403.08226
Fischer, D. A., Marcy, G. W., Butler, R. P., et al. 2008, ApJ, 675, 790
Fischer, D. A., Marcy, G. W., & Spronck, J. F. P. 2014, ApJS, 210, 5
Fischer, D. A., & Valenti, J. 2005, ApJ, 622, 1102
Folsom, C. P., Fossati, L., Wood, B. E., et al. 2018, MNRAS, 481, 5286
Foreman-Mackey, D., Hogg, D. W., Lang, D., & Goodman, J. 2013, PASP, 125, 306
Fulton, B. J. 2017, PhD thesis, Univ. Hawaii Manoa
Gaia Collaboration, Prusti, T., de Bruijne, J., H., J., et al. 2016, A&A, 595, A1
Gibson, S. R., Howard, A. W., Marcy, G. W., et al. 2016, Proc. SPIE, 9908, 990870
Guerrero, N. M., Seager, S., Huang, C. X., et al. 2021, ApJS, 254, 39
Handley, L. B., Howard, A. W., Rubenzahl, R. A., et al. 2024, AJ, 169, 212
Hansen, B. M. S., & Murray, N. 2012, ApJ, 751, 158
Howell, S. B., Everett, M. E., Sherry, W., Horch, E., & Ciardi, D. R. 2011, AJ, 142, 19
Izidoro, A., & Raymond, S. N. 2018, in Handbook of Exoplanets, ed. H. J. Deeg & J. A. Belmonte (Cham: Springer), 142
Izidoro, A., Raymond, S. N., Morbidelli, A., Hersant, F., & Pierens, A. 2015, ApJL, 800, L22
Kipping, D. M. 2013, MNRAS, 434, L51
Knudstrup, E., Gandolfi, D., Nowak, G., et al. 2023, MNRAS, 519, 5637
Li, G., Naoz, S., Kocsis, B., & Loeb, A. 2014, ApJ, 785, 116
Lin, D. N. C., & Papaloizou, J. 1986, ApJ, 309, 846
Lubin, J., Petigura, E. A., Van Zandt, J., et al. 2024, AJ, 168, 196
Lubin, J., Van Zandt, J., Holcomb, R., et al. 2022, AJ, 163, 101
Mahadevan, S., Ramsey, L., Bender, C., et al. 2012, Proc. SPIE, 8446, 84461S
Massey, F. J. 1951, JASA, 46, 68
Mayor, M., Marmier, M., Lovis, C., et al. 2011, arXiv:1109.2497
Naoz, S. 2016, ARA&A, 54, 441
Nielsen, E. L., De Rosa, R. J., Macintosh, B., et al. 2019, AJ, 158, 13
Osborn, H. P., Nowak, G., Hébrard, G., et al. 2023, MNRAS, 523, 3069
Pecaut, M. J., & Mamajek, E. E. 2013, ApJS, 208, 9
Pepe, F., Cristiani, S., Rebolo, R., et al. 2021, A&A, 645, A96
Petigura, E. A. 2015, PhD Thesis, Univ. California Berkeley
Petigura, E. A., Marcy, G. W., Winn, J. N., et al. 2018, AJ, 155, 89
Polanski, A. S., Lubin, J., Beard, C., et al. 2024, ApJS, 272, 32
Raghavan, D., McAlister, H. A., Henry, T. J., et al. 2010, ApJS, 190, 1
Ricker, G. R., Winn, J. N., Vanderspek, R., et al. 2015, JATIS, 1, 014003
Rogers, J. G., & Owen, J. E. 2021, MNRAS, 503, 1526
Rosenthal, L. J., Fulton, B. J., Hirsch, L. A., et al. 2021, ApJS, 255, 8
Rosenthal, L. J., Knutson, H. A., Chachan, Y., et al. 2022, ApJS, 262, 1
Schwab, C., Rakich, A., Gong, Q., et al. 2016, Proc. SPIE, 9908, 99087H
Schwarz, G. 1978, AnSta, 6, 461
Scott, N. J., Howell, S. B., Gnilka, C. L., et al. 2021, FrASS, 8, 138
Serrano, L. M., Gandolfi, D., Hoyer, S., et al. 2022, A&A, 667, A1
Van Zandt, J., & Petigura, E. 2024a, AJ, 167, 250
Van Zandt, J., & Petigura, E. A. 2024b, AJ, 168, 268
Van Zandt, J., Petigura, E. A., MacDougall, M., et al. 2023, AJ, 165, 60
Venner, A., An, Q., Huang, C. X., et al. 2024, MNRAS, 535, 90
Vogt, S. S., Allen, S. L., Bigelow, B. C., et al. 1994, Proc. SPIE, 2198, 362
Vogt, S. S., Burt, J., Meschiari, S., et al. 2015, ApJ, 814, 12
Vogt, S. S., Radovan, M., Kibrick, R., et al. 2014, PASP, 126, 359
Wallace, A. L., Casey, A. R., Brown, A. G. A., & Castro-Ginard, A. 2025, MNRAS, 536, 2485
Weiss, L. M., Isaacson, H., Howard, A. W., et al. 2024, ApJS, 270, 8
Winn, J. N., & Fabrycky, D. C. 2015, ARA&A, 53, 409
Winn, J. N., & Petigura, E. 2024, arXiv:2401.16451
Wittenmyer, R. A., Wang, S., Horner, J., et al. 2020, MNRAS, 492, 377
Wright, J. T., Marcy, G. W., Howard, A. W., et al. 2012, ApJ, 753, 160
Yee, S. W., Petigura, E. A., & von Braun, K. 2017, ApJ, 836, 77
Zhao, L. L., Kunovac, V., Brewer, J. M., et al. 2023, NatAs, 7, 198
Zhu, W. 2022, AJ, 164, 5
Zhu, W. 2024, RAA, 24, 045013
Zhu, W., & Wu, Y. 2018, AJ, 156, 92
Zink, J. K., & Howard, A. W. 2023, ApJL, 956, L29